remote sensing

MDPI

Article

Land Surface Phenology and Seasonality Using Cool Earthlight in Croplands of Eastern Africa and the Linkages to Crop Production

Woubet G. Alemu [1,*] and Geoffrey M. Henebry [1,2]

[1] Geospatial Sciences Center of Excellence, South Dakota State University, Brookings, SD 57007-3510, USA; geoffrey.henebry@sdstate.edu

[2] Department of Natural Resource Management, South Dakota State University, Brookings, SD 57007, USA

* Correspondence: woubet.alemu@sdstate.edu; Tel.: +1-605-592-1242

Received: 30 June 2017; Accepted: 29 August 2017; Published: 1 September 2017

Abstract: Across Eastern Africa, croplands cover 45 million ha. The regional economy is heavily dependent on small holder traditional rain-fed peasant agriculture (up to 90%), which is vulnerable to extreme weather events such as drought and floods that leads to food insecurity. Agricultural production in the region is moisture limited. Weather station data are scarce and access is limited, while optical satellite data are obscured by heavy clouds limiting their value to study cropland dynamics. Here, we characterized cropland dynamics in Eastern Africa for 2003–2015 using precipitation data from Tropical Rainfall Measuring Mission (TRMM) and a passive microwave dataset of land surface variables that blends data from the Advanced Microwave Scanning Radiometer (AMSR) on the Earth Observing System (AMSR-E) from 2002 to 2011 with data from AMSR2 from 2012 to 2015 with a Chinese microwave radiometer to fill the gap. These time series were analyzed in terms of either cumulative precipitable water vapor-days (CVDs) or cumulative actual evapotranspiration-days (CETaDs), rather than as days of the year. Time series of the land surface variables displayed unimodal seasonality at study sites in Ethiopia and South Sudan, in contrast to bimodality at sites in Tanzania. Interannual moisture variability was at its highest at the beginning of the growing season affecting planting times of crops, while it was lowest at the time of peak moisture. Actual evapotranspiration (ETa) from the simple surface energy balance (SSEB) model was sensitive to track both unimodal and bimodal rainfall patterns. ETa as a function of CETaD was better fitted by a quadratic model ($r^2 > 0.8$) than precipitable water vapor was by CVDs ($r^2 > 0.6$). Moisture time to peak (MTP) for the land surface variables showed strong, logical correspondence among variables ($r^2 > 0.73$). Land surface parameters responded to El Niño-Southern Oscillation and the Indian Ocean Dipole forcings. Area under the curve of the diel difference in vegetation optical depth showed correspondence to crop production and yield data collected by local offices, but not to the data reported at the national scale. A long-term seasonal Mann–Kendall rainfall trend showed a significant decrease for Ethiopia, while the decrement was not significant for Tanzania. While there is significant potential for passive microwave data to augment cropland status and food security monitoring efforts in the region, more research is needed before these data can be used in an operational environment.

Keywords: AMSR-E; AMSR2; passive microwave; rainfall; actual evapotranspiration; quadratic model; crop production

1. Introduction

Across Eastern Africa, croplands cover 45 million ha [1]. Ethiopia (ET) and Tanzania (TZ) are the two major crop producing countries in the region, accounting for 14 million ha and 13 million ha of

croplands, respectively [1]. The African economy is heavily dependent on small holder traditional rain-fed peasant agriculture (up to 90% in Eastern Africa), which is vulnerable to extreme weather events such as drought and floods [2–4]. Moreover, sluggish economic development in the region has been unable to feed the fast growing population, leading to chronic risk of regional food insecurity [5–7]. Food crops mainly produced in the region include maize, sorghum, wheat, barley, millet, rice, teff (a small grain produced and used primarily in Ethiopia), beans, and peas [8]. Farming systems in Ethiopia are mainly highland temperate mixed and maize mixed, while in Tanzania it is mainly maize mixed, and in South Sudan cereal-root crop mixed [8]. The highland temperate mixed farming system produces small grains, such as wheat, barley, teff, and livestock. The maize mixed farming system mainly produces maize and livestock. Production in the cereal-root crop mixed farming system is based on vegetables, animal products, and cereals, such as maize, sorghum, and millet.

Primary climate variables, such as pressure, temperature, and precipitation, are forced in part by intrinsic dynamical modes of the climate system. These modes include the Arctic Oscillation (AO) and its Southern Hemisphere counterpart, the Antarctic Oscillation (AAO)—these are also known as the Northern and Southern Annular Mode (NAM and SAM), respectively, the El Niño-Southern Oscillation (ENSO), the Pacific Decadal Oscillation (PDO), and the Indian Ocean Dipole (IOD), among others [9,10]. Due to these dynamic modes, climatic variation in one part of the planet can be teleconnected to a geographically distant part of the planet. Many observed climatic changes can be related to one or more of the leading modes [9]. Crop production in Eastern Africa is based on traditional farming practices, and it is solely rain-fed and is, therefore, susceptible to the weather extremes associated climatic mode anomalies, particularly to the IOD and ENSO modes [11].

Rainfall over Eastern Africa responds to global scale circulation patterns linked to conditions in both the Pacific and Indian Oceans, such as the ENSO and the IOD [10,12–15]. Rainfall in the region is influenced more by IOD than ENSO [10,15–18]. Niño3, one of many complementary ENSO indices, is the sea surface temperature (SST) anomaly averaged over the region spanning 150–90°W, 5°S–5°N [19]. El Niño events have usually produced anomalously drier conditions in Eastern Africa, while La Niña events are associated with wetter conditions [20–22]. IOD is represented by an anomalous SST gradient between the Western Equatorial Indian Ocean (50–70°E and 10°S–10°N) and the Southeastern Equatorial Indian Ocean (90–110°E and 10°S–0°N) [23,24]. This gradient is named the Dipole Mode Index (DMI). When the DMI is positive, the phenomenon is referred to as a positive IOD, and vice versa. A positive IOD is associated with wetter periods in Eastern Africa; whereas a negative IOD means drier periods [12,15,20,21,25] in this region.

In Ethiopia, there is a minor rainy season in March called *belg*, while the main rainy season falls between June and September, known as *kiremt*. Tanzania experiences a shorter rainy season between October and December and longer rains between March and May; meanwhile, in South Sudan, the rainy season spans from May to October. Regional rainfall trends have been decreasing, but they are highly variable in space and time [26]. Thus, precipitation variability is a principal contributor to food insecurity in Eastern Africa. A study in Western Africa found that the timing and length of the sowing period depend on the arrival of rains and soil moisture [27]. During the past century, shortage of rainfall in Ethiopia led to recurrent drought, which resulted in substantial shortfalls in agricultural production triggering food insecurity, which led to multiple episodes of famine, especially in the eastern half of the country [28]. However, highland regions receive excess rainfall concentrated into the few months of their rainy season, which leads to flooding and soil erosion that, in turn, deplete soil nutrients and reduce crop productivity [7].

Solar irradiance and temperature are important factors for agricultural crop productivity. In Eastern African highlands (12°S–15°N), the rainy season is accompanied by high cloud cover that reduces insolation and thus temperature. Mathan [29] found that the number of days for the completion of germination, plant height, leaf area index, grain, straw, and total dry matter yield for sorghum were related to the sunshine hours. Grain and straw yields were positively related to accumulated heat units (accumulated growing degree-days, AGDD) [29]. Sunlight quality and quantity

available for plant growth is dependent on atmospheric conditions and seasonality [30]. These factors (and others), in addition to moisture, contribute to the long history of food insecurity in Eastern Africa.

To address issues of food insecurity, we need a comprehensive understanding of cropland dynamics for major commodity crops. Cropland dynamics includes the land use and land cover change in cropland regions as observed at coarser spatial resolutions that cannot resolve crop type due to spatial heterogeneity and spectral mixing. Land surface phenology (LSP) plays an important role in monitoring cropland dynamics. LSP deals with the timing of vegetated land surface dynamics as observed by satellite remote sensors, particularly at spatial resolutions and extents relevant to meteorological processes in the atmospheric boundary layer [31,32]. Phenological studies integrate climate–biosphere relationships as the timing of vegetation lifecycle events is influenced by temperature and precipitation [33–36]. Remotely sensed vegetation indices (VIs) such as the normalized difference vegetation index (NDVI) [37] have been widely utilized for agricultural mapping and monitoring [38–42]. The Famine Early Warning System Network (FEWS NET), which is funded by the United States Agency for International Development (USAID) and implemented by the United States Geological Survey (USGS), uses NDVI-based measures of cropland activity as part of its integrated early warning system for food security and drought monitoring in food-insecure regions of the world, such as Eastern Africa, Western Africa, Southern Africa, Central America and the Caribbean, and Central Asia [43]. FAO's Global Information and Early Warning System (GIEWS) uses NDVI data to detect vegetation health as a proxy for crop production [44]. Land surface dynamics in tropical Eastern Africa are less well characterized than those in the major crop growing regions of developed nations. We used our previous experience of using passive microwave data to track temperate cropland dynamics in the spring wheat belts of the Northern Hemisphere [45–47] as reference areas to contrast with the cropland dynamics of tropical Eastern Africa.

Many studies have used vegetation indices (VIs) derived from visible and near infrared (VNIR) sensors to study LSP in terms of days of the year [48–50], but far fewer using thermal time [31,45–47,51,52]. However, tropical croplands generally do not have temperature constraints; rather, they are strongly dependent on rainfall and moisture for crop growth and development. Therefore, to characterize LSP and land surface seasonality (LSS) in the region, we have used moisture time measured as cumulative water vapor-days (CVDs) based on a spatially continuous variable—atmospheric precipitable water vapor—that is available from passive microwave data.

In addition, the skies over Eastern Africa are obscured by heavy seasonal clouds and dust contamination, reducing insolation, and surface air temperature as well as limiting intensive observation of the vegetated land surface by VNIR sensors. To characterize cropland dynamics in Eastern Africa, specifically in Ethiopia, Tanzania, and the newer nation of South Sudan, we used a blended dataset of enhanced land surface variables produced from the passive microwave radiometers AMSR-E (Advanced Microwave Scanning Radiometer on EOS) and AMSR2 (hereafter simply AMSR) [53], rainfall data from TRMM (Tropical Rainfall Measuring Mission), and ETa (actual evapotranspiration) data estimated from the simple surface energy balance model (SSEB) [54,55].

2. Study Region, Data and Methodology

2.1. Study Region

Across Eastern Africa, croplands cover 45 million ha. Our study focuses on croplands in the two major crop producing countries in the region, Ethiopia (ET) and Tanzania (TZ), and South Sudan (SS). Ethiopia and Tanzania contain 14 million ha and 13 million ha of croplands, respectively. South Sudan, however, remains a bit of a mystery; it is still too new and torn by civil strife to appear in the FAO agricultural databases.

Specific AMSR pixels were selected in these countries in a two-step process. We first developed cropland cover stability map in Eastern Africa for cropland class (12) from the International Geosphere Biosphere Program (IGBP) land cover scheme using the MODIS fractional land cover layer in MCD12C1

for 2003–2012. We calculated the maximum, minimum, and mean land cover percentage over the study period and then displayed the maximum, mean, and range in the red, green, and blue color planes, respectively [56]. Thus, yellow shows temporally stable core areas of the cropland class; white shows temporally unstable core areas; magenta displays unstable peripheral areas; black shows where the croplands class did not occur 2003–2012 (Figure 1). The MODIS land cover product, which has a spatial resolution of 0.05 degrees, could not resolve finely fragmented croplands in the study region. Thus, while we used the MODIS data as general guidance, we used the finer resolution imagery available in Google Earth Image to select and check visually our study sites. We have identified 100 study AMSR cropland pixels, 14 in Tanzania, 6 in South Sudan, and 80 in Ethiopia (Figure 1).

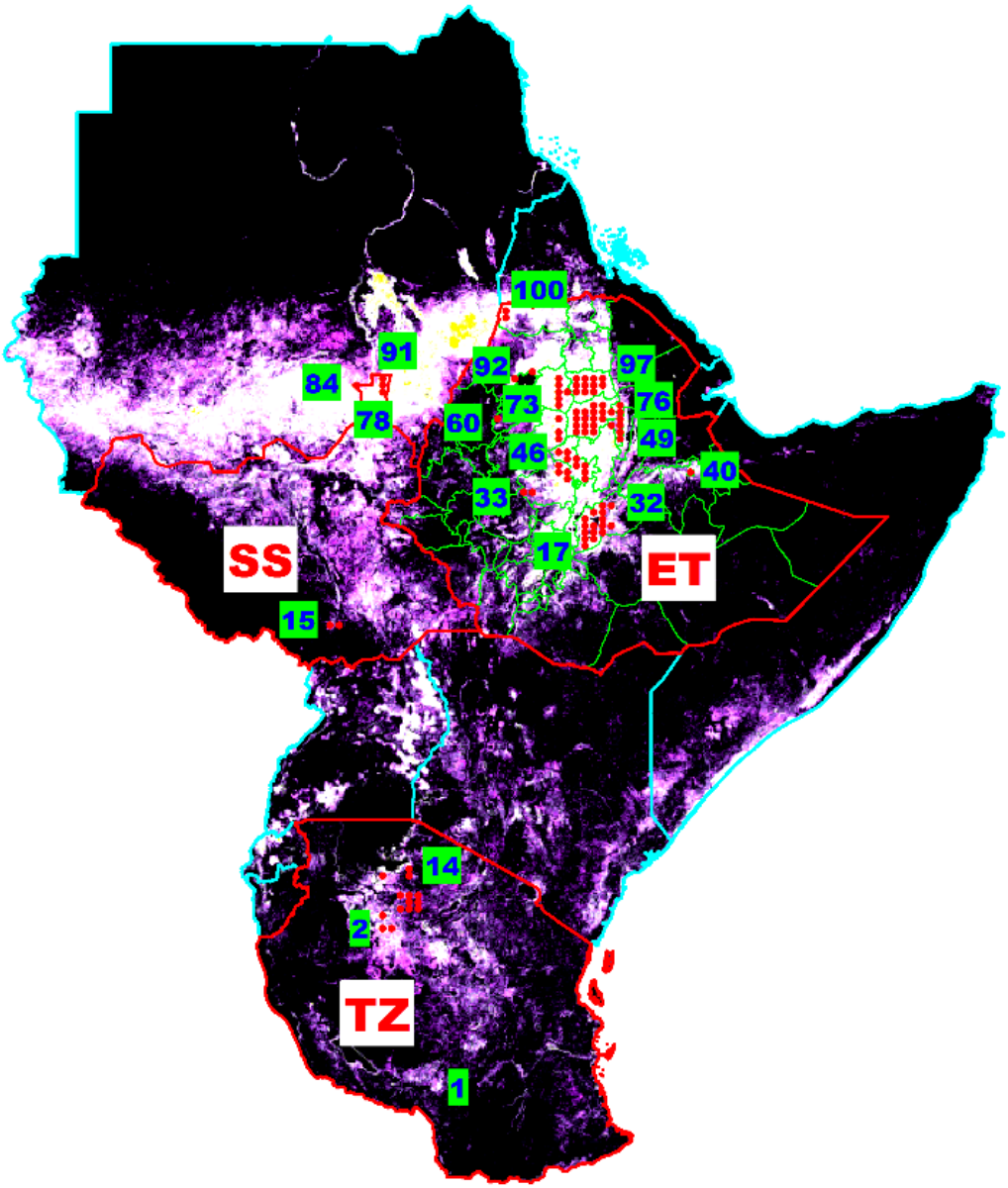

Figure 1. Cropland class stability map in Eastern Africa for 2003–2012. Yellow shows stable core cropland areas; white displays unstable core areas; magenta displays unstable peripheral areas; black shows where croplands do not occur in the study period. Superimposed are 100 AMSR pixels (red dots) selected on dominant cropland areas. Pixels are numbered from S to N and then from W to E (all numbers are not labeled due to space limitations).

We subset from the MODIS product the four major IGBP land cover types in the study region (cropland, cropland/natural vegetation mosaic, savanna, and grassland) to calculate the proportions of these land covers within each AMSR pixel (Figure 2a). Note that these land cover classes constitute nearly all of the land cover in the study area.

To provide additional land cover data at finer spatial resolution, we subset the Landsat 7 ETM+ 30 m resolution Global Land Cover data layer (tree cover, bare ground, and waterbodies) [57] to calculate the proportions of these land cover within each AMSR pixel. The tree cover and bare ground were raster layers with proportion of these covers per pixel (1–100%) in 2010, while the water layer was a thematic layer where the ground was persistently water from 2000 to 2012. The tree cover and bare ground that were within the AMSR study pixels were averaged separately. Proportion of waterbodies within the AMSR pixel were also calculated. Thus, a given AMSR pixel can have proportional tree cover, bare ground, water, and residual land cover. Any residual percentage of land cover could be cropland, shrubland, grassland, and other land cover class. Note that croplands can appear as bare ground much of the year. Moreover, since we purposely selected AMSR pixels dominated by croplands as evident in Google Earth imagery, the residual land cover should be mainly cropland, but there could also be a mixture of grassland and shrubland. Among our study pixels, there are two sites (92 and 98) that have a considerable proportion of waterbody—25% and 30%, respectively (Figure 2b). These sites are located near Lake Tana, the largest lake in Ethiopia. There are some other sites with up to 30% of tree cover and bare ground combined.

2.2. Data

2.2.1. Remote Sensing Data

We have primarily used variables retrieved from the passive microwave data of AMSR-E and AMSR2. The AMSR-E was launched onboard the NASA-EOS Aqua satellite in May 2002 and operated successfully for more than 9 years before it stopped properly functioning in October 2011, due to failure of the rotating antenna's spin mechanism. Since May 2012, its measurement legacy has been continued by AMSR2, which is the improved version of AMSR-E with similar functionality. AMSR2 is onboard the Japan Aerospace Exploration Agency (JAXA) Global Change Observation Mission 1st-Water (GCOM-W1) "SHIZUKU" satellite. We used the blended AMSR-E/AMSR2 dataset developed by the Numerical Terradynamic Simulation Group (NTSG) at the University of Montana [53]. The NTSG filled the gap between the AMSR-E and AMSR2 sensors using brightness temperature observations from the Microwave Radiation Imager (MWRI) onboard the Chinese FengYun 3B (FY3B) satellite that was launched in November 2010 [53]. The AMSRs record observations twice daily (daytime ~1330 and nighttime ~0130). The gridded data products have a spatial resolution of 25 km. The NTSG-blended AMSR dataset includes up to two observations per day from June 2002 to December 2015 of surface air temperatures (ta; ~2 m height), fractional open water inundation (fw), vegetation canopy transmittance (tc) at 10.65 GHz, volumetric soil moisture (vsm; $\leq$2 cm soil depth), and atmosphere precipitable water vapor (V) for the total column [53,58]. The data set will continue to be extended as long as AMSR2 continues to produce data (J.S. Kimball, personal communication). These products are critical in regions where meteorological stations are sparse and high quality rainfall measurements are missing or unavailable [59,60], such as Eastern Africa. The finer temporal resolution of passive microwave datasets is also another significant advantage to monitor cropland dynamics, given the rapid pace of plant growth and development. The major drawback of passive microwave datasets is their coarse spatial resolution (25 km) relative to the region's characteristic small farm field sizes and fragmented croplands.

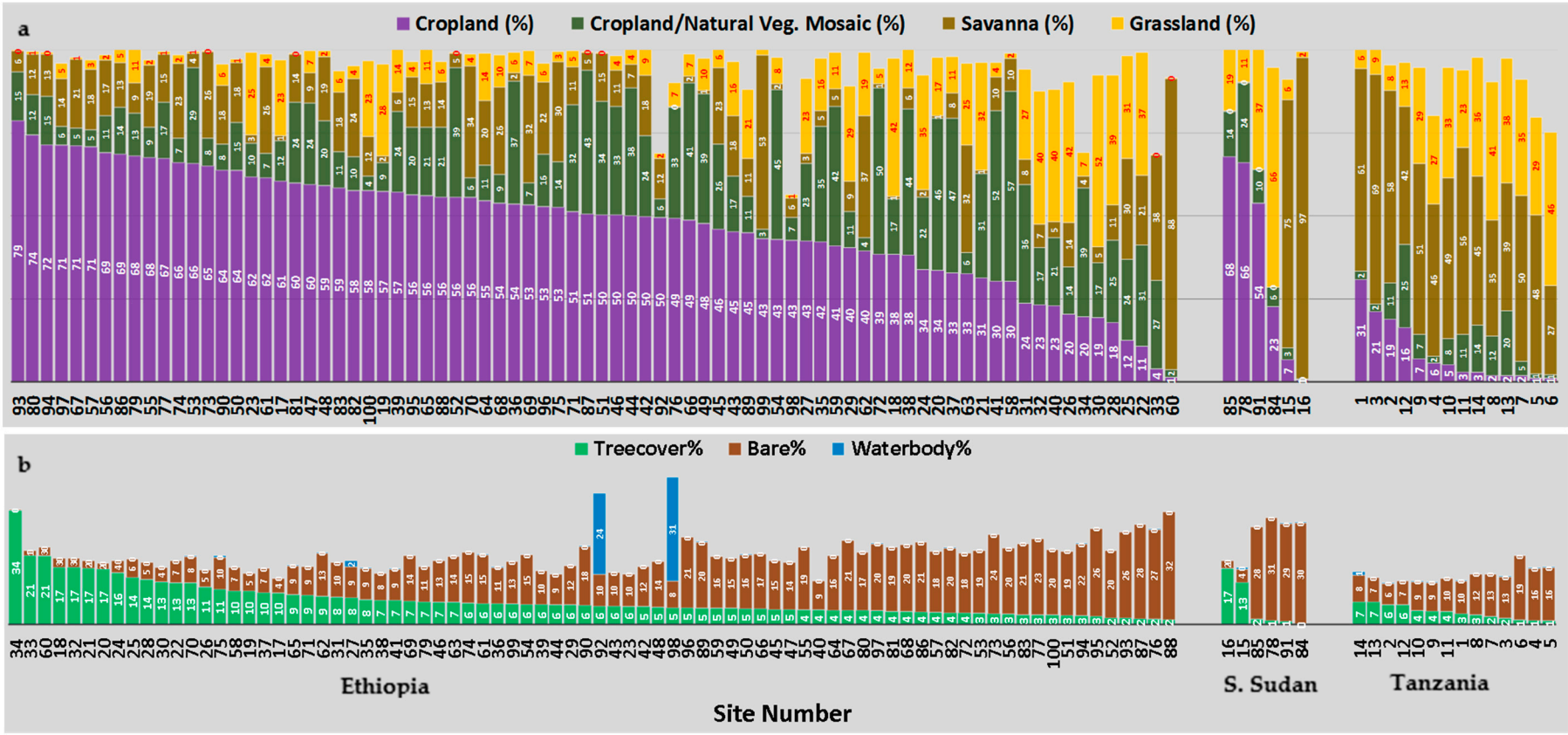

Figure 2. (**a**) Mean percentage cropland (purple), cropland/natural vegetation mosaic (green), savanna (dark gold) and grassland (gold) cover in percent for 2003–2012 from the MODIS IGBP Land Cover Type 1 Percent Product at 0.05 degree spatial resolution MCD12C1 [61]. (**b**) Percent tree cover, bare ground, and waterbody from the Landsat ETM+ 30 m resolution Global Land Cover product [57]. Figure 1 shows the latitudinal distributions of the study sites and countries in which they are found numbered by latitude from south (1) to north (100). The X-axis indicates study sites, sorted by (**a**) MODIS cropland % and (**b**) Landsat treecover % from high to low. Land cover % values are labeled on the respective bars.

The second dataset used in this study is rainfall data from TRMM, which combines active and passive microwave sensors. A joint US–Japan space mission, TRMM was launched in November 1997 to monitor and study tropical rainfall (50°N–50°S latitude), and officially ended in April 2015. Its measurement legacy has been continued by the Global Precipitation Measurement (GPM) mission launched on February 2014. The TRMM Multi-satellite Precipitation Analysis (TMPA) version 7 (TRMM 3B42 (V7)) is a rainfall dataset developed by NASA that provides TRMM-adjusted gridded rainfall rate (mm/h) estimates from multiple satellites at 3-hourly temporal and 0.25-degree spatial resolution [62]. We used the daily accumulated rainfall product that is derived from the 3-hourly product (TRMM 3B42 (V7)-daily) [63]. We also used the NOAA Global Precipitation Climatology Center (GPCC) long-term monthly rainfall data [64] for the regional rainfall trend analysis.

We used actual evapotranspiration (ETa) data estimated from the simple surface energy balance model (SSEB) [54,55]. These data have a 1 km spatial resolution and a 10-day (dekadal) temporal resolution. The data used as input to the SSEB model include the MODIS 8-day Land Surface Temperature product at 1-km resolution (MOD11A2); the MODIS 16-day NDVI product at 250-m resolution (MOD13Q1), and the global 1-degree reference evapotranspiration (ET_0) based on NOAA's 6-hourly Global Data Assimilation Systems (GDAS) model output.

We used the monthly time series of the Optimum Interpolation Sea Surface Temperature (OISST.v2) Niño3 index from NOAA National Weather Service Climate Prediction Center [65] to identify El Niño and La Niña events during our study period. To identify positive and negative Indian Ocean Dipole (IOD) phenomena, we used the Dipole Mode Index (DMI) time series from Japan Agency for Marine-Earth Science and Technology (JAMSTEC), which is based on the Hadley Centre Sea Ice and Sea Surface Temperature (HadISST) dataset [66].

2.2.2. Crop Production Data

We gathered crop production and yield data for the Amhara Region of Ethiopia at two administrative levels: woredas (smaller) and zones (larger). Some zones were also included from the Oromia Region, Ethiopia. The woredas for which crop production and yield data were analyzed include Dejen, Enemay, and Enebise Sar Midir in the West Gojjam Zone, Simada and Lay Gaint in the South Gondar Zone, Jama, Legehida, Legambo, and Delanta in the South Wollo Zone, and Wadla and Gidan in the North Wollo Zone. The woreda level data were collected by the Amhara National Regional State Bureau of Agriculture (ANRS BoA) for 2014. The zone level data were taken from agricultural sample survey reports for Ethiopia for the 2003–2014 period [67–69] organized by the Ethiopian Central Statistical Agency (CSA). These zones include South Wollo, East Gojjam, North Wollo, South Gondar, North Shewa, West Shewa, and Arsi. The reports are for "private peasant holdings" by season of production, organized at three levels (national, regional, and zonal levels), and each level includes crop area, crop production, and yield by crop type. More than 85% of Ethiopian population is a rural resident dependent mainly on small holder subsistence agriculture. Commercial farms in Ethiopia are few and are limited to the remote peripheral lowlands of the country. We also obtained woreda (district) level crop production and yield data for 2014 from the Amhara National Regional State Bureau of Agriculture (ANSR BoA) organized by the Zonal agricultural offices. We also use gathered regional level Tanzanian National Sample Census of Agriculture crop production data for 2008 for eight regions, namely, Njombe, Nzega, Shinyanga Rural, Shinyanga Urban, Kishapu, Meatu, Maswa, and Bariadi [70].

2.3. Methods

We analyzed 14 full years (2003–2015) of twice-daily AMSR data. We applied an 8-day retrospective moving average filter to the daytime and nighttime AMSR data separately, to minimize data gaps due to orbit and swath width. We then averaged the daytime and nighttime values for all variables except surface air temperature (ta) to obtain one value per 24 h. The ta time series were processed into growing degree-days (GDDs), the daily thermal-time increment above a certain

threshold (base temperature) for plant growth [31,71,72]. GDDs were calculated from the AMSR air temperature (ta) data with a base temperature of 0 °C (=273.15 K) as follows:

$$\mathrm{GDD} = \max\left[\frac{t_{ASC} + t_{DES}}{2} - 273.15,\ 0\right] \quad (1)$$

where t_{ASC} and t_{DES} are ascending and descending pass temperatures, which corresponds roughly to the maximum and minimum daily temperatures.

We have previously modeled the seasonal course of NDVI in temperate croplands as a quadratic function of accumulated growing degree-days [45–47]. However, for the moisture-limited croplands of Tropical Eastern Africa, this approach is not appropriate since temperature is not the key limiting factor in the timing and progress of crop growth.

To illustrate the differential seasonality of croplands, Figure 3 displays GDDs and precipitable water vapor (V) at two cropland sites, one in Zegie, Ethiopia, and the other in Saratov, Russia, and reveals the quasi-periodic behavior of GDD versus V in both croplands. At the tropical site, a larger dynamic range of V and smaller dynamic range of GDD within the year is evident compared to the temperate site (Figure 3). This pattern reflects that moisture is the key limiting factor in the tropical croplands, and temperature is limiting in the temperate croplands. Brown & de Beurs [27] successfully applied a quadratic model in Western Africa croplands to characterize cropland NDVI as a function of accumulated relative humidity.

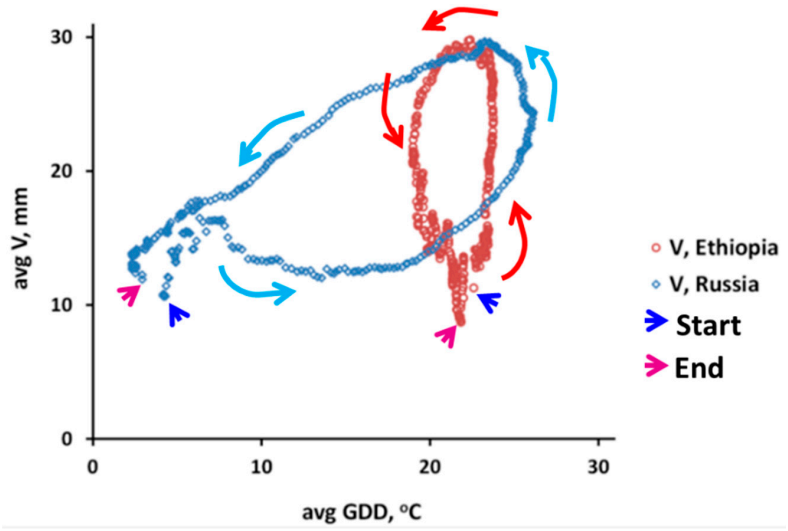

Figure 3. Scatterplot of 30-day retrospective moving average of mean AMSR-E atmospheric water vapor (V) as a function of average growing degree-days (GDDs) for Zegie, Ethiopia (maroon circles), and Saratov, Russia (blue diamonds), for the 2003–2010 period. Blue arrows indicate initial points in January, while magenta arrows indicate endpoints of the annual cycle in December. Red arrows show intra-annual cycles of V for Zegie, ET, and cyan arrows for Saratov, RU. Note the relative dynamical range of the variables.

Rainfall in Eastern Africa is erratic and sporadic. From a daily TRMM rainfall data, we calculated 8-day retrospective cumulative rainfall for our study. In contrast, precipitable water vapor (V) is a continuous spatiotemporal field. Thus, we analyzed the time series of biophysical and climatic variables as a function of precipitable water vapor. Cumulative water vapor days (CVDs) are the simple summation of AMSR V throughout the whole year. That is, the passage of days is weighted by the quantity of V occurring that day:

$$\mathrm{CVD}_t = \mathrm{CVD}_{t-1} + \mathrm{V}_t \quad (2)$$

where V_t is daily precipitable water vapor at time t. The concept is analogous to the use of accumulated growing degree-day (AGDD) to study cropland dynamics in the temperature-limited temperate croplands.

Vegetation optical depth (VOD) was calculated as the negative logarithm of vegetation transmittance (tc) at 10.65 GHz:

$$\mathrm{VOD} = -\log_e(\mathrm{tc}) = -\ln(\mathrm{tc}). \quad (3)$$

The actual evapotranspiration (ETa) estimates were a retrospective summation for every 10 days (dekad). To match the time scale, we produced comparable AMSR and TRMM dekadal datasets by summing the daily data. We compare the ETa data with the AMSR and TRMM datasets. We have cumulative annual ETa and V data (designated as CETaDd [Cumulative ETa Dekad] and CVDd [Cumulative V Dekad]) to characterize all our study variables as a function of CETaDd and CVDd:

$$\mathrm{CETaDd}_t = \mathrm{CETaDd}_{t-1} + \mathrm{ETa}_t \quad (4)$$

$$\mathrm{CVDd}_t = \mathrm{CVDd}_{t-1} + \mathrm{V}_t \quad (5)$$

where ETa is dekadal actual evapotranspiration, and V_t is dekadal atmospheric precipitable water vapor at time t.

To characterize the seasonal progression of moisture, we fitted the ETa from SSEB model product and V from AMSR as a quadratic functions of CETaDd and CVDd, respectively:

$$\mathrm{ETa}_t = \alpha + \beta \times \mathrm{CETaDd}_t - \gamma \times \mathrm{CETaDd}_t{}^2 \quad (6)$$

$$\mathrm{V}_t = \alpha + \beta \times \mathrm{CVDd}_t - \gamma \times \mathrm{CVDd}_t{}^2 \quad (7)$$

where the intercept α is the start of observation period ETa/V value, the linear parameter β affects the slope, and the quadratic parameter γ controls the curvature. Our model is an arched quadratic in shape; thus, the sign of the β coefficient is positive, while the sign of the γ coefficient is negative.

At sites with two rainfall seasons, the ETa and V time series display bimodal patterns. At these sites, we fitted two separate quadratic models, one for each rainfall season. From the observed data, the breakpoints for these two rainfall seasons were more or less similar in time and space, but different between the northern and southern hemispheres. Therefore, for the quadratic model fit, we divided the observations into two growing season phases. The first phase for Ethiopia and South Sudan ran from DOY 001–201 (1 January–20 July) and the second phase ran from DOY 202–365 (21 July–31 December). In Tanzania, the phases ran from DOY 182–052 (1 July–21 February) and DOY 053–181 (22 February–30 June).

We modeled characteristics of each biophysical and climatic variable in terms of cumulative moisture time. We determined peak height (PH) of each variable using the seasonal maxima, and the corresponding moisture time to peak (MTP) was measured in CVDs. We also calculated the PH lag time between biophysical and climatic variables.

For the ENSO analysis, we standardized the Niño3 index data using a 30-year (1986–2015) climatology to obtain the mean and standard deviation [19,73]. We then filtered the standardized data using a 5-month retrospective moving average [19] (Figure 11). If the index value exceeded ± 1 for at least two consecutive months in the rainy season, that year was labeled as El Niño for positive deviations or La Niña for negative deviations [19]. A similar approach was applied to the DMI time series with the positive (or negative) IOD mode indicated by the DMI remaining above 1 (or below -1) for at least two consecutive months in the rainy season [19]. Any given year may experience a positive (El Niño) or negative (La Niña) or neutral ENSO mode and a positive or negative or neutral IOD mode. Therefore, there are nine possible combinations of these events in a given year (Table 1).

Table 1. Classification of years when El Niño or La Niña and/or positive or negative Indian Ocean dipole occurred.

IOD/ENSO	Negative IOD	Neutral	Positive IOD
El Niño	−/+	0/+	+/+
Neutral	−/0 *	0/0	+/0
La Niña	−/−	0/−	+/−

* 0 = Neutral.

We examined crop production and yield data for the Amhara Region of Ethiopia at two administrative levels: woredas (smaller) and zones (larger). Some zones were also included from the Oromia Region, Ethiopia. We used the assumption that crop biomass and crop evapotranspiration are linked to crop production to link cropland LSP to crop production and yield statistical data in the region. We calculated the area under the curve (AUC) for the growing season VOD as a proxy for crop biomass and the AUC for the growing season VOD diel difference (VODdd) as a proxy for crop evapotranspiration: $VODdd = VOD_{DSC} - VOD_{ASC}$, where VOD_{DSC} and VOD_{ASC} are the descending and ascending VOD, respectively. We calculated separate AUCs for the VODs derived from the ascending and descending orbits, in addition to the average VOD. We assessed the relationship between the growing season maximum VOD and the crop production data, since growing season maximum NDVI has corresponded with crop production data in past research [74]. Actual evapotranspiration data from the simplified surface energy balance (SSEB) model was used to link it with crop production and yield data. One way to determine the AUC cut-points (the points to start and end the integration) was using the variation of volumetric soil moisture (vsm). The vsm starts to rise continuously as the main rainfall season began, and then starts to drop as moisture was drawn down by growing crops. The moisture started to rise again as the crops dried out (Figure 4). The AUC was integrated between these soil moisture cut points, and the crop production and yield data were linked to the AUCs using simple linear regression.

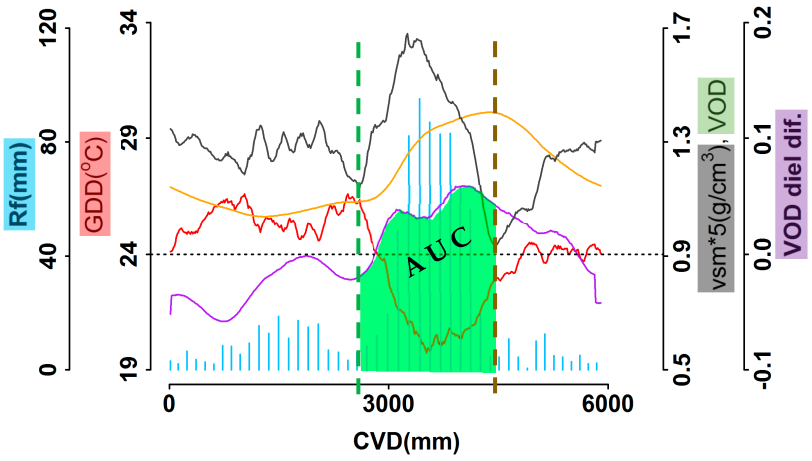

Figure 4. AUC (area under the curve) of VODdd (vegetation optical depth diel difference; green area under the purple curve) at AMSR pixel cropland site in Ethiopia (Site 82). The cut points were determined based on the seasonality of volumetric soil moisture.

Even though crop production statistical data lower level of aggregation and AMSR data spatial resolution were comparable in size, they may not necessarily overlap each other. Therefore, before trying to link crop production and the derived LSP and LSS metrics (AUC, maximum VOD, and rainfall), we normalized these variables by area. We multiplied the reported crop production data at a given season (CP_s) by a factor of cultivated area in a given administrative division during this season (CA_s) divided by the total area in that administrative division (TAA): $CP_s \times CA_s/TAA$.

This formulation presumes the crop production is evenly distributed across the administrative division. Although we know that agriculture is not evenly distributed, it is a reasonable first-order assumption given the scale differences of these data. We normalized the phenology or seasonality metric (PSM) by multiplying by a factor of the overlap area between the AMSR pixel and the administrative division (OA) divided by the total AMSR pixel area (TPA): PSM $\times$ OA/TPA.

3. Results

3.1. Land Surface Seasonalities of Precipitable Water Vapor

Precipitable water vapor (V) in the northwestern and central parts of the croplands in the Ethiopian highlands displayed weak unimodal seasonality and stronger intra-seasonal variation (Figure 5). Croplands in the drier lowlands of Northern South Sudan experienced strong unimodal V seasonality and minimal intra-seasonal variation. Croplands in Tanzania showed clear bimodal V seasonality as well as strong intra-seasonal variation.

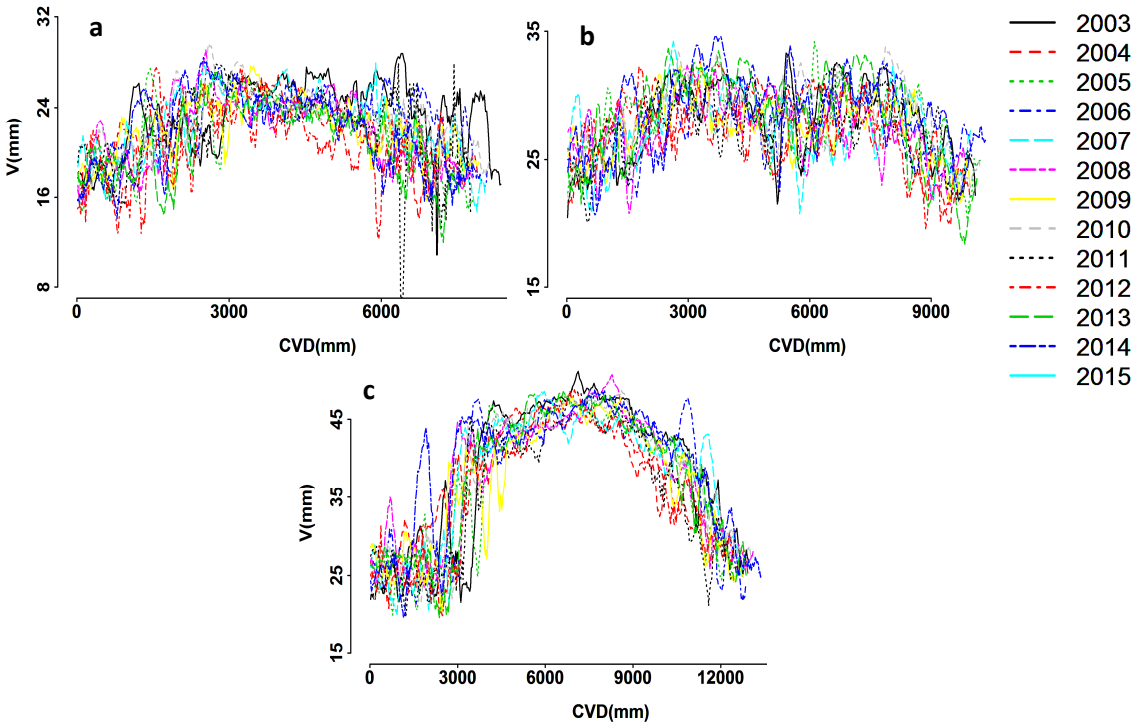

Figure 5. V time series graphs for ET ((**a**) site #60), TZ ((**b**) #6), and SS ((**c**) #85) for 2003–2015. Note differences in scaling of axes.

3.2. Land Surface Seasonality and Phenology of AMSR Land Parameters & TRMM Rainfall

AMSR land surface parameters and TRMM rainfall time series displayed a unimodal seasonality in Ethiopia and South Sudan, while there is clear bimodality for sites in Tanzania, which is in line with the climatic seasonality, particularly for the rainfall, of the respective countries described in the introduction.

In the drier lowlands of South Sudan, there was high intra-annual dynamic range of V and soil moisture (vsm) and higher magnitude of V and GDD (Figure 6b, #78) compared to the highlands of Ethiopia (Figure 6a, #73) or Tanzania (Figure 6c, #14). Rainfall and VOD had higher magnitude in the humid highlands of Ethiopia followed by Tanzania. In Ethiopia, vsm rose as the rainy season started, then sharply dropped as VOD increased due to soil moisture drawdown by growing vegetation, and finally bounced back as the canopy senesced.

GDD dropped during the rainfall and active vegetation growing season, despite the overhead sun during this time of the year. First, the rainfall season in this part of the world is characterized by a heavy cloud deck that reflects back much of the insolation, thereby reducing the amount of light available at the surface for plant growth [75–77]. Second, evapotranspiration from actively growing crops cools down the surrounding air through evaporative cooling yielding a lower Bowen Ratio [46].

The behavior of VOD as a function of CVDs exhibited distinctive land surface phenology trajectories. During the growing season, VODs rapidly ascended to a unimodal peak value and declined gradually. The pace of fractional green vegetation cover development was quicker than during its disappearance (Figure 7). The diel difference in the VOD (VOD_{dd}) was highest during the rainy season due to high evapotranspiration in daytime by actively growing crop vegetation.

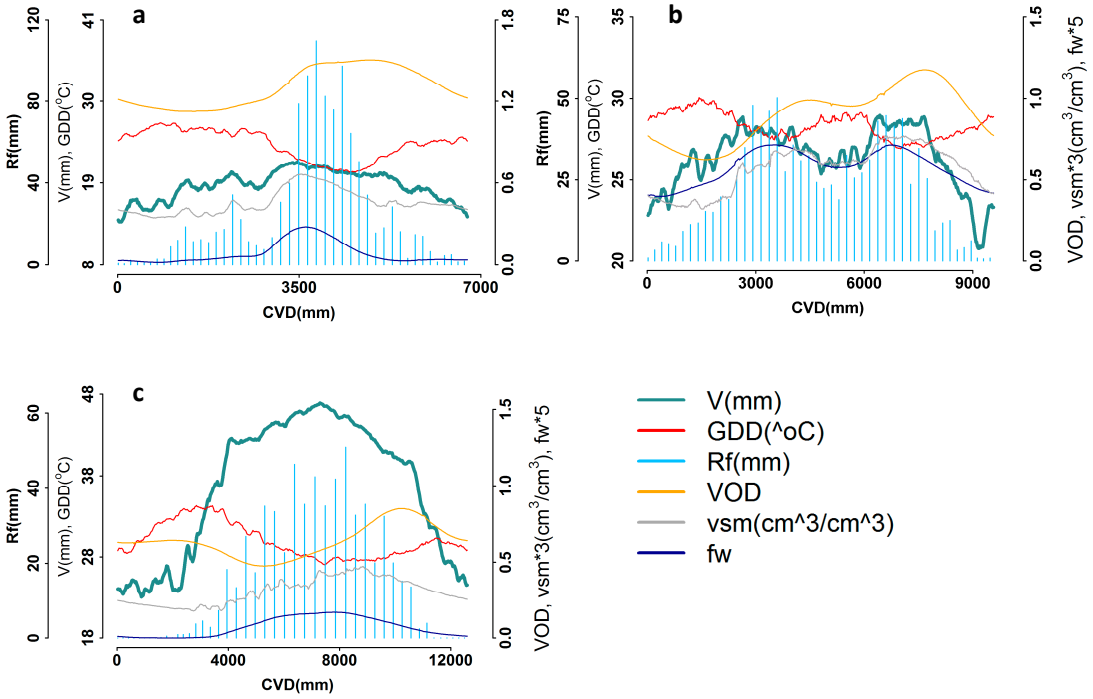

Figure 6. Line graphs and bars of multiyear average (2003–2015) of AMSR V, GDD, vsm, fw, and VOD (10.65 GHz) with TRMM rainfall (Rf) as a function of cumulative vapor days (CVDs) for an AMSR pixel at sites in Ethiopia ((**a**) #73), South Sudan ((**b**) #78), and Tanzania ((**c**) #14). Note differences in scaling of axes.

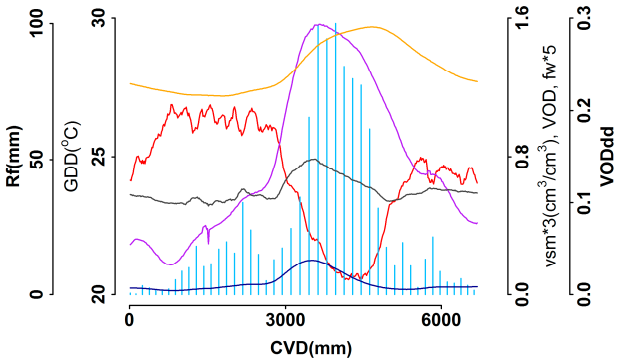

Figure 7. Average GDD, vsm, and (VODdd) VOD diel difference (#93, Ethiopia) time series graphs for 2003–2015. Purple indicates VODdd, while the legend for other variables is the same as that in Figure 5.

3.3. Land Surface Seasonality of Soil Moisture

Interannual moisture variability was at its highest at the beginning of the growing season affecting planting times of crops, while it was at its lowest at the time of peak moisture. Variability was higher for South Sudan sites (Figure 8c, #91) followed by Tanzania (Figure 8b, #5), while it was lower for Ethiopia (Figure 8a, #35).

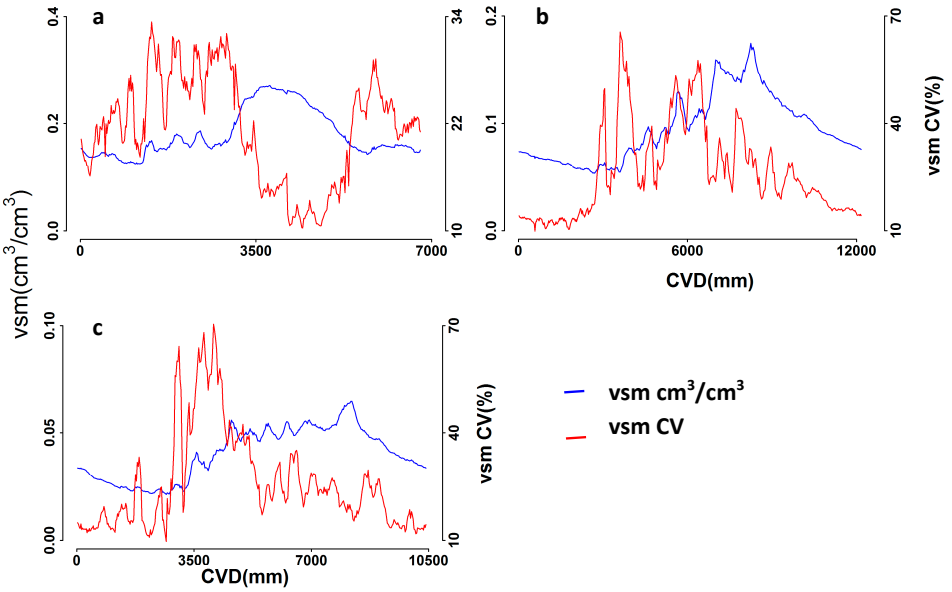

Figure 8. Average (2003–2015) vsm superimposed with its interannual CV (%) and standard error bars for (**a**) site #35 in Ethiopia), (**b**) #5 in South Sudan, and (**c**) #91 in Tanzania. Note differences in scaling of axes.

3.4. Land Surface Seasonality of Actual Evapotranspiration

Actual evapotranspiration (ETa) from the simple surface energy balance model closely tracked the rainfall pattern in time and space. ETa was very sensitive to track both the unimodal and bimodal rainfall patterns (Figure 9). ETa increased while there was sufficient soil moisture for evapotranspiration demand and reached its peak slightly later than the peak rainfall period (~2 weeks; Table 3). The ETa from the active growing vegetation and the wet ground in the rainfall season cooled down the surrounding surface air (evaporative cooling) resulting in lower GDD. The relationship among these land surface and atmospheric variables held true for both the unimodal and bimodal growing season dynamics. ETa was higher at lowland cropland sites that received enough moisture to meet evapotranspiration demand.

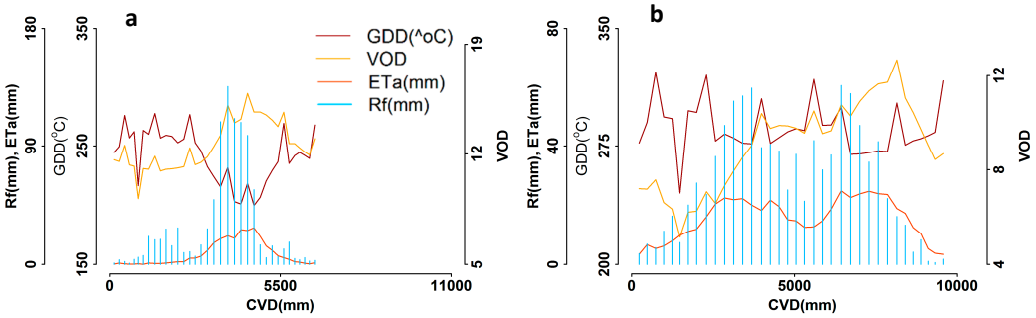

Figure 9. Time series of MODIS rainfall, SSEB ETa, and AMSR GDD and VOD for (**a**) #87 in Ethiopia and (**b**) #14 in Tanzania for 2003–2015.

The quadratic model fits for ETa and V for sites with unimodal growing season were strong (Figure 10a,b). The quadratic fits of ETa and V at sites with bimodal growing seasons were fitted with two separate models, one for each growing season (Figure 10c,d). These fits were generally strong, but the fits of the second (main) growing season were better ($r^2 > 0.8$) than those of the first growing season ($r^2 > 0.6$). Fits with ETa were better than those with V. ETa displayed sharper seasonal dynamics, appearing more responsive to rainfall, soil moisture, and vegetation moisture compared to V.

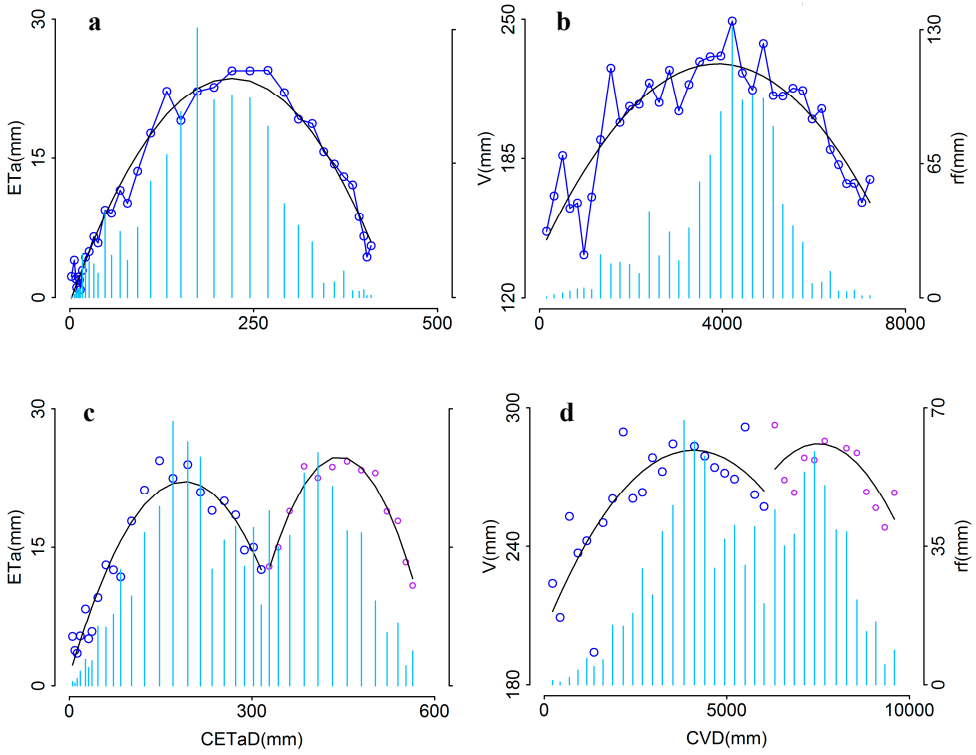

Figure 10. Quadratic model fits for average growing season (2003–2015) at a unimodal site (#48) in Ethiopia for (**a**) ETa ($r^2 = 0.97$) and (**b**) V ($r^2 = 0.79$) and at a bimodal site (#14) in Tanzania for (**c**) ETa ($r^2 = 0.93, 0.96$) and (**d**) V ($r^2 = 0.63, 0.38$). Blue bars are rainfall (rf) graphs for the same period. Note the relative dynamics of ETa and V in relation to rf, and the differences in axis scaling by site.

3.5. El Niño/Southern Oscillation and the Indian Ocean Dipole

Five of the nine possible ENSO/IOD events combinations were observed during the study period, and no instance of a negative IOD was observed except briefly during the short rainfall season of Tanzania in 2016. Note that the long rainy season in Tanzania in 2016 coincided with a positive IOD and an El Niño year (Figure 11, Table 2).

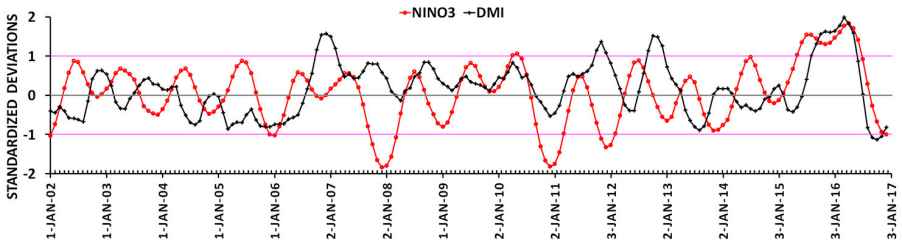

Figure 11. Thirty years (1986–2015) standardized anomaly five months retrospective smoothed time series plots of NIÑO3 (red) and DMI (black) for 2002–2016. Pink horizontal lines represent ± standard deviation.

Table 2. Classification of years when El Niño or La Niña and/or positive or negative Indian Ocean dipole occurred.

IOD/ENSO	−ve IOD	Neutral	+ve IOD
El Niño	–	–	2015, 2016
Neutral	–	2003–2005, 2008–2009, 2013–2014	2006, 2012
La Niña	–	2007, 2010	2011

3.6. Land Surface Phenology Linkages to Crop Production Statistics

Woreda level data collected from local offices were better fit (r^2 = 0.60) by a logarithmic curve (Figure 12a), suggesting saturation, than by a line (r^2 = 0.57; data not shown). VODdd AUC showed a weak but significant linear correspondence to crop yield data with an r^2 of 0.25 (Figure 12b).

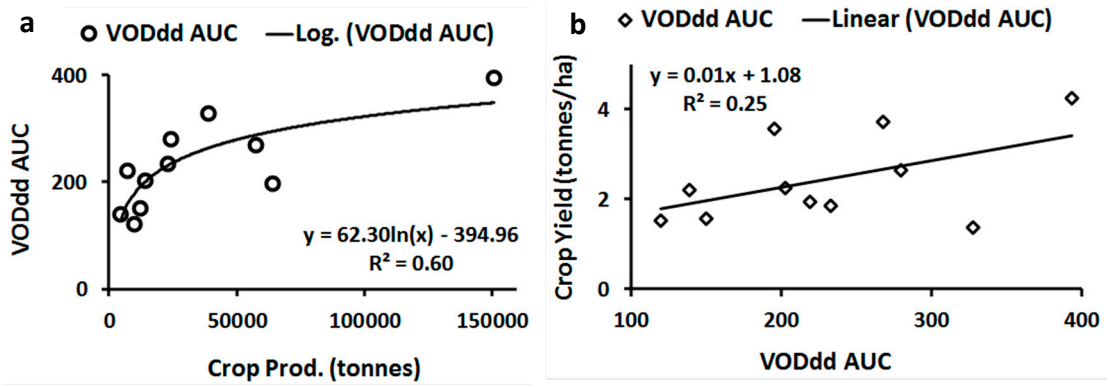

Figure 12. Relationships between area under VOD_{dd} curve and statistical data for (**a**) crop production and (**b**) crop yield at the woreda level in the Amhara Region in Northwestern Ethiopia for 2014. Both fits are significant at $p < 0.01$.

The Zonal level CSA data from the highland agricultural areas of the Amhara and Oromia Regions for 2003–2008 and 2010 (2009 data were not available) indicated that crop production substantially increased (Figure 13). There is weaker evidence of a cultivated area increase during the same period in these zones. The VODdd AUC also showed that there is very little change during this period, except in 2010. The North Wollo Zone showed consistently lower crop production, cultivated area, and VODdd AUC time series. The Zones in Figure 13c were clustered into two general groups. The lower VODdd AUC value clusters were North Wollo, South Wollo, and East Gojjam, while the remaining four zones make up the higher VODdd AUC value clusters. The VODdd AUC displayed weak but significant correspondence with crop production data at the zone level in five of seven zones. Significant relationships were found in West Shewa, North Shewa, East Gojjam, South Wollo, and North Wollo Zones, with coefficients of determination ranging from 0.25 to 0.72. No significant relationship was found in either Arsi or South Gondar Zones (data not shown). The VODdd AUC also showed significant correspondence with rainfall data in the same five zones ($0.29 < r^2 < 0.73$), but not in South Gondar or Arsi. Maximum VOD showed a significant correspondence with crop production data in four of seven zones (West Shewa, East Gojjam, South Wollo, and North Wollo).

The VODdd AUC data with crop production statistical data at the regional level in Tanzania for 2008 showed a positive correspondence across regions with r^2 of 0.67 (Figure 14b). Since our sample size was small, this correspondence was dominated by one or two extreme values. Increasing sample size could reduce the uncertainty of the correspondence, but these ground level data are limited. The VODdd AUC tracks the relative pattern of regional crop production statistical data in six of eight regions in the western half of Tanzania (Figure 14a). The six regions include Njombe, Nzega, Shinyanga Urban, Kishapu, Maswa, and Bariadi.

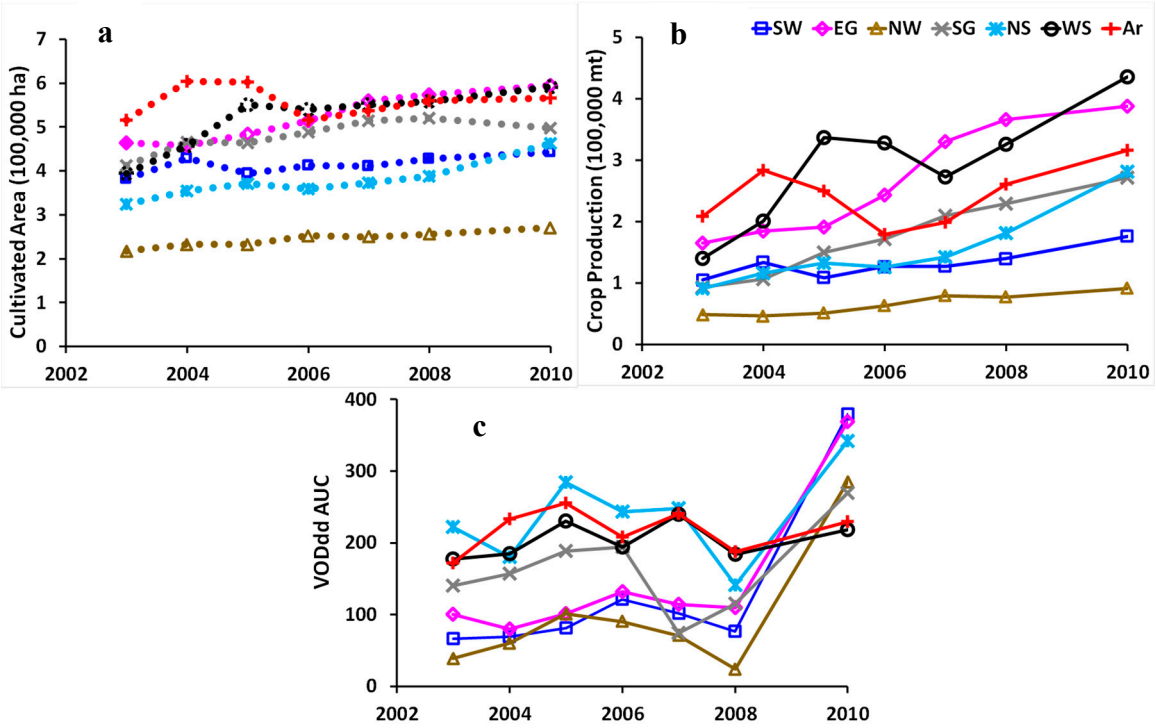

Figure 13. Time series graphs of (**a**) cultivated area, (**b**) crop production, and (**c**) VODdd AUC in five zones (SW = South Wollo, EG = East Gojjam, NW = North Wollo, SG = South Gondar, NS = North Shewa, WS = West Shewa, and Ar = Arsi. Note the differences in rates of change of the crop production data relative to the VODdd AUC satellite derived data.

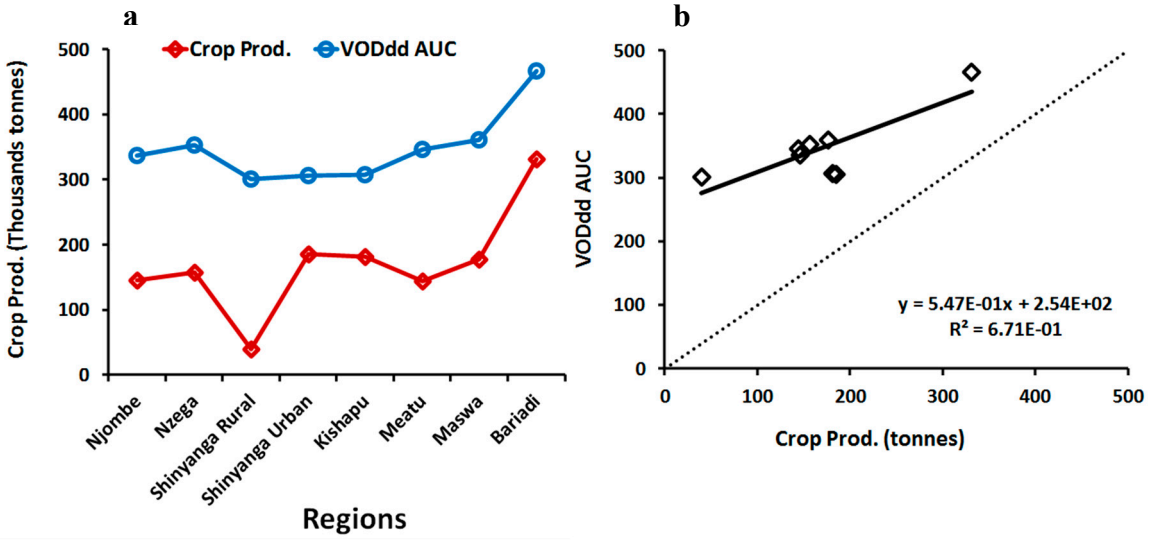

Figure 14. Graphs of (**a**) crop production statistical data and VODdd AUC and (**b**) their linear regression fit across regions in Tanzania for 2008. The fit was significant at $p < 0.01$.

4. Discussion

4.1. Seasonal Peak and Moisture Time to Peak (MTP) for Land Surface Phenologies and Seasonalities

Moisture time to peak (MTP) for land surface phenologies and land surface seasonalities showed strong correspondence between and among land surface parameters derived from AMSR, rainfall from TRMM, and ETa from SSEB with $r^2 > 0.73$ for most variables in the Ethiopian study sites (Figure 15).

Furthermore, lags between variables exhibited logical sequencing. For example, the MTP for rainfall lagged the MTP for precipitable water vapor by about five weeks (Figure 15; Table 3). The MTP for volumetric soil moisture leads the MTP for rainfall due to earlier wetting and saturation period of the soil ahead of peak rainfall period. In addition, soil moisture was drawn down by actively growing crop vegetation, decreasing the soil moisture. The soil moisture saturation period depends, in part, on soil texture and type, land cover type, and land use. The MTP for VOD lags the MTPs for rainfall and volumetric soil moisture by about seven and eleven weeks, respectively. In Ethiopia, VOD peaked in mid-October, while rainfall peaked in mid-August. The peak timing for some variables occurred around the same time, e.g., the MTP for VOD diel difference and the MTT (Moisture Time to Trough) for GDD (growing degree-days), which is the CVDs (cumulative precipitable water vapor-days) to the seasonal lowest GDD). GDD dropped to its lowest point due to evaporative cooling from growing crops. There were no apparent relationships among the MTPs of variables in the South Sudan sites due to few data points and heterogeneous land cover. A similar pattern was found for the Tanzanian sites, where some sites support a double growing season and others support a single growing season.

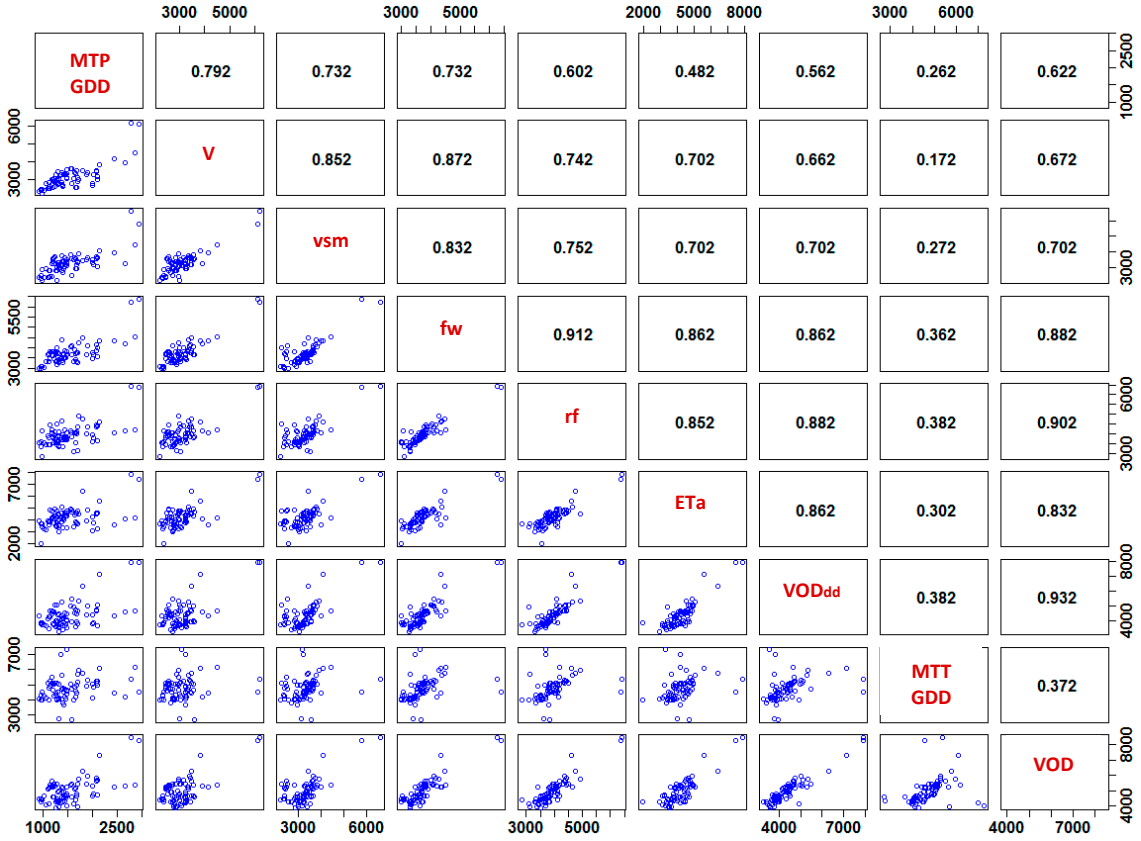

Figure 15. Moisture Time to Peak (MTP) or Moisture Time to Trough (MTT) for cropland land surface variables in Ethiopia for 2003–2015 ($r^2 > 0.8$). The variables listed in the diagonal of the figure from top-left to bottom-right include moisture time to peak or trough for MTP for growing degree-days (MTP GDD), precipitable water vapor (V), volumetric soil moisture (vsm), fractional open water (fw), rainfall (rf), actual evapotranspiration (ETa), vegetation optical depth diel difference (VODdd), MTT for growing degree-day (MTT GDD), and vegetation optical depth (VOD). Note that peak rf lags peak V, peak soil moisture, and peak VOD, but VODdd lags peak rf. Upper panel shows the Pearson correlation coefficients. All correlations were significant with $p < 0.01$. To identify variables combination for any given plot or r-value, make horizontal and vertical lines towards the diagonal line of the square matrix containing the variables.

Table 3. MTP lag in weeks between each variable averaged in space and time (2003–2015) for Ethiopian sites. Note that these lags can vary in space and time for particular sites.

	MTP GDD	MTP V	MTP vsm	MTP fw	MTP Rf	MTP ETa	MTP VODdd	MTT GDD	MTP VOD
MTP GDD		11	12	15	16	18	20	20	24
MTP V			1	4	5	7	9	9	12
MTP vsm				3	4	6	7	8	11
MTP fw					1	3	4	5	8
MTP Rf						2	3	4	7
MTP ETa							2	2	5
MTP VODdd								0	4
MTT GDD									3
MTP VOD									

4.2. AMSR Variables Response to El Niña Southern Oscillation and Indian Ocean Dipole Modes

The positive IOD year of 2006 brought heavy rainfall to the region (Figure 16, Table 2), resulting in major nationwide flooding in Ethiopia [78–82]. Moreover, the rainfall was concentrated in a few months of the rainy season causing unprecedented flooding. The floods affected 8 out of the country's 11 administrative regions and led to acute food insecurity for at least 10 million people [79,81]. This extreme event caused internal mass displacement and considerable damage to property and infrastructure leading to acute food shortage for more than 7 million people [79,81].

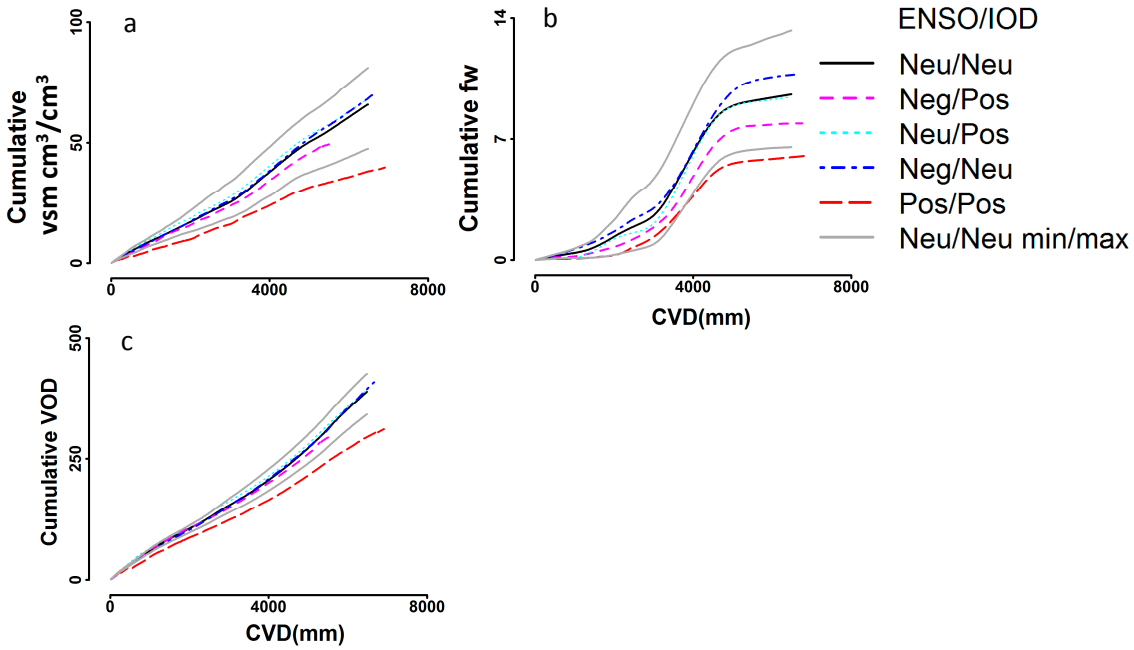

Figure 16. Time series of (**a**) cumulative volumetric soil moisture (vsm), (**b**) cumulative fractional water (fw), and (**c**) cumulative vegetation optical depth (VOD) in Central Ethiopia. The neutral ENSO/IOD years are represented by the black line, while the maxima and minima of this combination are represented by gray. The rest shows other possible combinations of ENSO/IOD.

In 2010, a La Niña year, there was heavy rainfall and flooding in Ethiopia [83]. The flooding affected nearly 1 million people across several administrative regions [84]. Rainfall in 2010 was above normal but distributed throughout the rainy season. Thus, the flooding and associated damage in Ethiopia were not as severe as in 2006 [79,83]. Soil moisture and fractional water were high in these

positive IOD and La Niña years compared to the neutral years, while the VOD looked similar to the neutral years (Figure 16).

The worst drought in over 30 years occurred in 2015. It claimed human and animal life and devastated crop production, especially in Eastern Ethiopia [85–89]. More than 10 million people (~ 10% of Ethiopia's population) were in need of food assistance [86,88]. This year was both an El Niño and a positive IOD year (Figure 11; Table 2). Even though the effect of El Niño and positive IOD may have been expected to cancel each other out [15,25], the severe drought of 2015 might be due to the three months of the El Niño event occurring before the positive IOD mode (in 2015 NINO3 > 1 occurred three months earlier than DMI > 1; Figure 16). Soil moisture (Figure 16a) and fractional water (Figure 16b) in 2015 were well below the minimum boundary envelope of the neutral years. Since the severe drought devastated crop production, VOD in 2015 (Figure 16c; red color) was well below that of the minimum boundary of the neutral years. In 2016, a La Niña year, most parts of Eastern Africa received heavy rainfall [89].

4.3. Crop Production Responses to Biophysical Factors

The logarithmic fit of the AUC of the VOD diel difference to the crop production data (Figure 12a) may result from VOD saturation, exaggerated crop production reports, and/or spatial extent disagreement between the satellite product and the crop production areal unit unresolved by the normalization procedure. Jones et al. [90] found that there is evidence of VOD signal saturation at higher biomass levels, but less is known about the diel difference of the VOD.

The Zone level CSA (Central Statistical Agency) crop production statistical data substantial increment in the highland agricultural areas of the Amhara and Oromia Regions for 2003–2010 was not supported by the VODdd AUC data (Figure 13). In some parts of Ethiopia 2010 was a flood year; however, the increment of the VODdd AUC in 2010 may have arisen the more even distribution of rainfall throughout the rainy season that, in turn, may have supported good crop growth and production. Consistently lower values for crop production, cultivated area, and VODdd AUC time series in the North Wollo Zone may result from it being drier and more degraded than other study sites. Not surprisingly, North Wollo is one of the more food-insecure zones in Ethiopia [91]. The VODdd AUC time series data appear to differentiate between drier and more mesic Zones: trajectories for the drier North and South Wollo Zones clustered with lower VODdd AUC values, in contrast to the clusters of the more mesic zones (Figure 13c).

In general, rainfall, VODdd AUC, VOD AUC, and VODmax did not exhibit noticeable increases during the study period (2003–2015). However, small holder agricultural crop production from the Ethiopian CSA in these zones has reportedly more than doubled in just eight years. Based on this governmental report, crop production grew at an annual rate of 6.5%, while the population growth was 2.6% over the same period of time. Yet, a paradox arises in that while crop production has apparently increased, millions have been food-insecure every year during the study period, including more than 10 million in the 2015 drought year [85,86].

Uncertainties in the national statistical data are not well characterized. In Ethiopia, administrative offices below the federal level lack organized historical datasets, and access to data at these offices is difficult. However, we also acknowledge that uncertainties also arise in the remote sensing data due to the mixture of other land covers with croplands within the 625 km^2 of each AMSR pixel, and potential biases arising from differences in the areal distribution of croplands within woredas that were not addressed by the normalization procedures.

FAO-harvested area and crop production country-level data [1,92] for Ethiopia and Tanzania were analyzed to better understand agricultural activity in the region. Note that such data are mainly collected from governmental agencies and thus may be subjected to bias. In Eastern Africa, institutional changes have been affecting agricultural land ownership and crop production through land policy reforms. Even though these institutional changes happen over longer time spans, they brought some

apparently abrupt changes on the agricultural sector (Figure 17). In contrast, rainfall variability has been the major driver for short-term fluctuations in agricultural crop production [28,93].

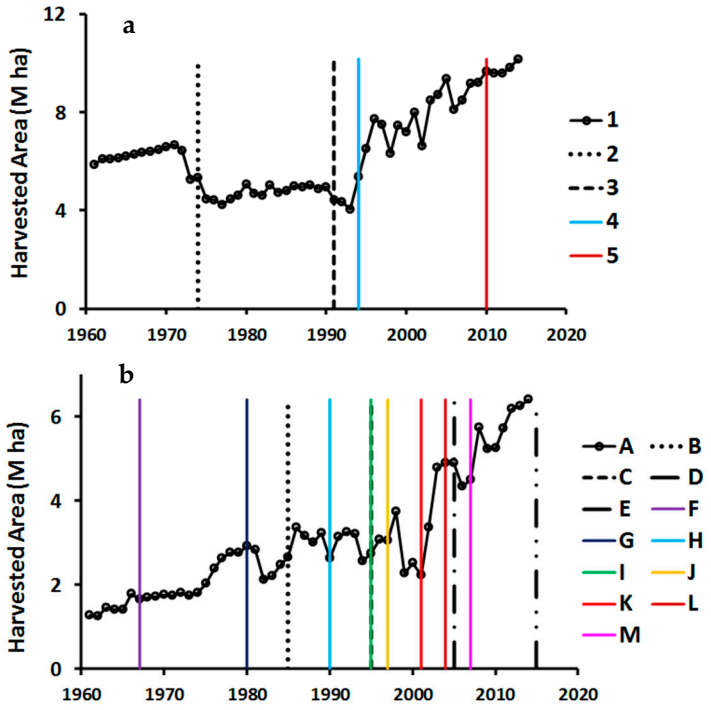

Figure 17. Harvested area time series graphs for (**a**) Ethiopia and (**b**) Tanzania overlaid with institutional change (black lines) and major land reform (colored lines) periods for 1961–2014. Periods are described in Appendix A, Table A1.

It is not clear why harvested area in Ethiopia drastically fell in the early 1970s, if those decreases are indeed real. However, some literature has claimed that around the end of Haile Selassie's rule (1930–1974), land was distributed by the crown to members of the military and those who were loyal to the regime, resulting in a concentration of land in the hands of few in the society [94]. Some of this cropland may have been idled as a result of institutional change, as has been observed elsewhere [33].

The FAO long-term data showed a tremendous crop production increment in Ethiopia in the 1990s and onwards compared to that of Tanzania. Generally, the production growth rate can be modeled using an exponential growth rate (r^2 = 0.78 for Ethiopia and r^2 = 0.90 for Tanzania; Figure 18). However, in Ethiopia since 2009, the increment has accelerated beyond exponential growth. Crop production as a function of harvested area is well fitted with a linear curve for Tanzania for 1961–2014, but with an exponential curve for Ethiopia for 1961–2008. However, since 2009, production statistics accelerated while harvested area saturated, and the exponential growth curve can no longer explain this correspondence, which casts doubt on the reported crop production figures.

The crop production and yield data showed a general correspondence with climate modes in both countries. The climate modes were annual averages to align them with crop production and yield data. This may have an adverse effect on the seasonal dynamics of climate modes that positive and negative extremes that occur in a given year may cancel out each other. Crop production and yield was at its minimum during El Nino/La Nina and positive/negative IOD years, while there were larger crop productions and yield during normal ENSO/IOD years (Figure 19). It appears that crop production and yield was more influenced by abnormal IOD than ENSO.

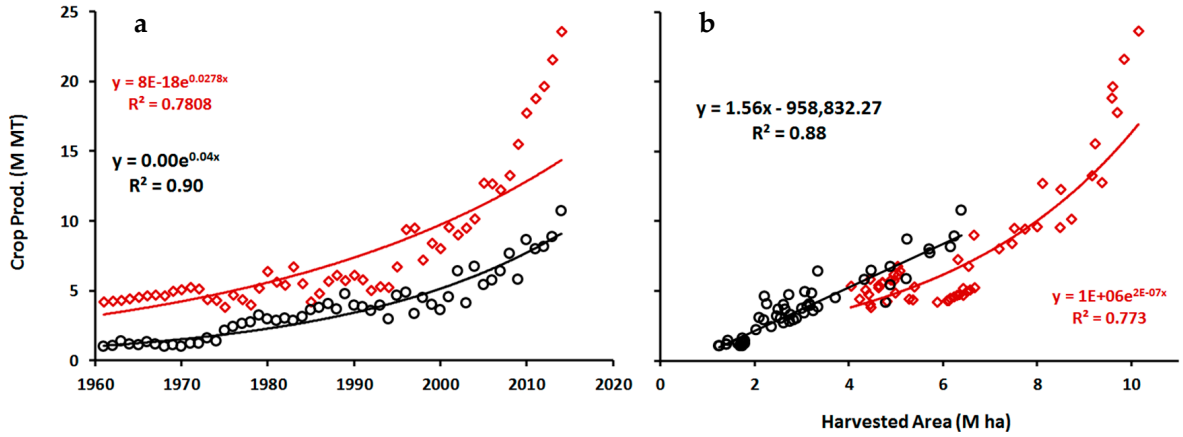

Figure 18. (**a**) Time series graphs of national annual crop production data in Ethiopia and Tanzania for 1993–2015. Source: [1]. Note the exponential growth rate of crop production data in Ethiopian relative to that of Tanzania. (**b**) Exponential fit of crop production as a function of harvested area for Ethiopia (red squares) and linear fit of that of Tanzania (black circles) for 1961–2014. Note the inability of the exponential curve to explain this relationship in Ethiopia that crop production tremendously increases while harvested area saturates.

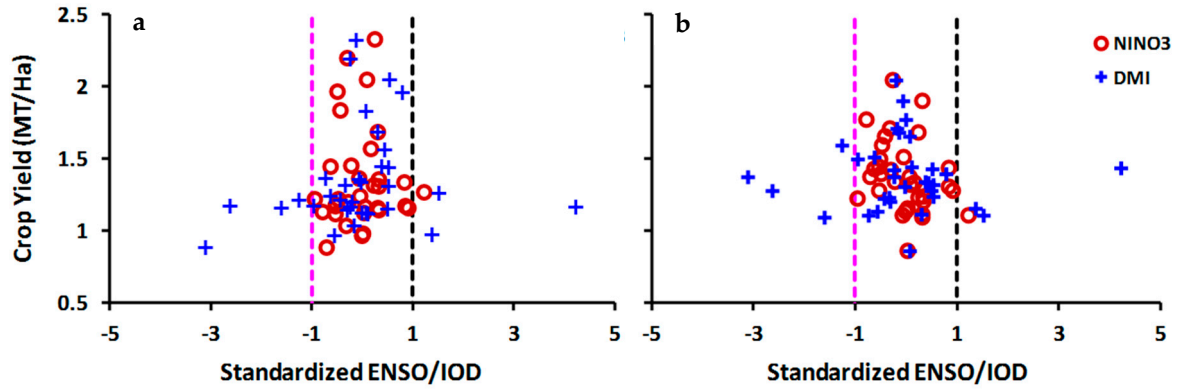

Figure 19. Crop yield in metric ton per hectare (MT/ha) as a function of climate modes in (**a**) Ethiopia and (**b**) Tanzania for 1982–2014. Note that the climate modes are annual averages from their respective standardized monthly indices.

Previously, we observed that VODmax exhibited strong correspondence with NDVI max ($r^2 > 0.8$) for cropland sites in Northern Eurasia [45]. A long-term (1988–2008) global vegetation biomass change study on major world biomes found correspondence between VOD and production of major crops [95]. Passive microwave data products have been shown to be relevant to the study of tropical cropland dynamics, but further studies are needed for these data to be used confidently and effectively. Such studies would best incorporate independent measurements (or estimates) of crop production and crop yield at the local level. In this step, crop production and yield data with uncertainty or errors resulting from insufficient knowledge about data collection protocols, statistical processing, and/or politically motivated data manipulation should be avoided.

4.4. Seasonal Kendall Trend Test on Long-Term Rainfall Data

Since crop production in Eastern Africa is strongly dependent on rainfall, we also investigated the long-term rainfall trend (1961–2016) [64] in both Ethiopia and Tanzania using the nonparametric Seasonal Kendall trend test (Figure 20) [96]. The rainfall data in Ethiopia for February (S = −282, $p = 0.046$) as well as for July (S = −366, $p = 0.010$) showed a significant ($p < 0.05$) negative trend according to the Seasonal Kendall test. Thus, the global trend for the entire series was significant (S = −1326, $p = 0.007$) (Figure 20a; Appendix B.1). Seasonal Sen's slope estimate yielded a slope of −11.2 mm/decade for Ethiopia. Rainfall data in Tanzania did not exhibit a significant trend for any month. Thus, the global trend for the entire series was not significant at $p < 0.05$ (S = −810, $p = 0.098$) (Figure 20b, Appendix B.2). For Tanzania, the Seasonal Sen's slope estimate yielded a slope of −4.3 mm/decade.

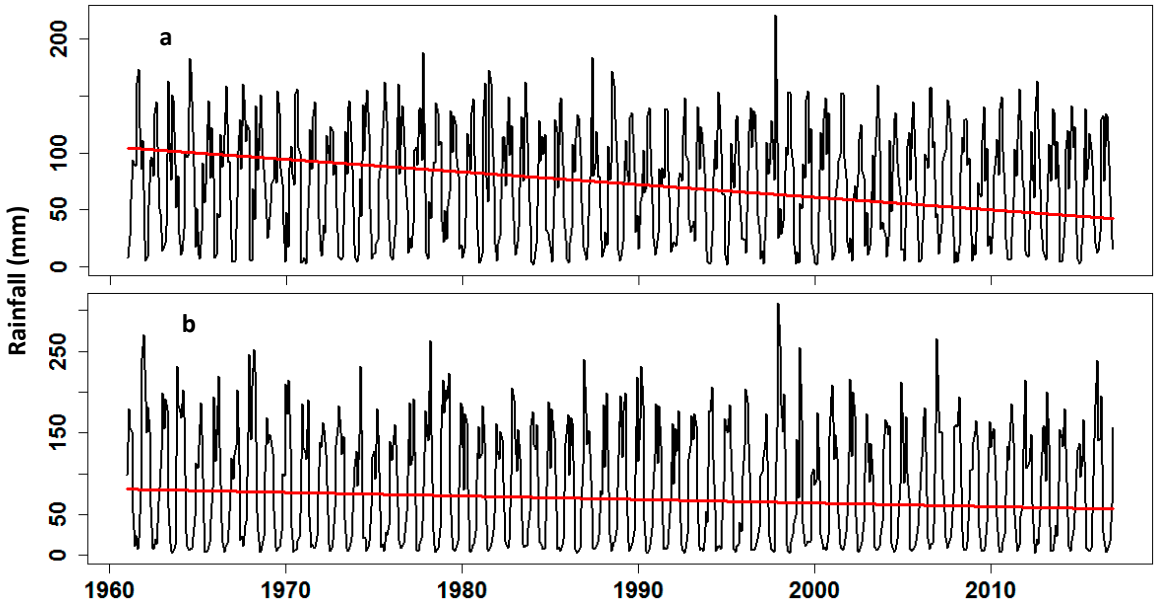

Figure 20. Seasonal Kendall rainfall trend with Seasonal Sen's slope for (**a**) Ethiopia and (**b**) Tanzania for 1961–2016. Ethiopia exhibited a significant decrease in rainfall of more than 11 mm/decade ($p = 0.007$), but the decrease in Tanzania was not significant at $p < 0.05$ ($p = 0.098$).

5. Conclusions and Recommendations

The economies of Eastern Africa are heavily dependent on traditional rain-fed agriculture that is vulnerable to extreme weather events, such as drought and floods. Even in the absence of conflict, this region has been one of the most food-insecure parts of the world over the past three decades or more. Weather station data are scarce and difficult to obtain, while optical satellite data are limited by obscuring clouds. Satellite passive microwave data are less sensitive to clouds and atmospheric effects. Therefore, we explored using passive microwave data to study cropland dynamics in Ethiopia, Tanzania, and South Sudan. Since crop production in the region is moisture limited, seasonal dynamics of the microwave datasets were characterized as functions of cumulative moisture, in contrast to the commonly used day-of-year or accumulated growing degree-days in temperate areas.

The microwave data were able to track cropland dynamics in time and space. Soil moisture was sensitive to rainfall and crop cover: it started to rise when rainfall commenced and attain its peak during the peak rainfall season, then sharply dropped during the active vegetation growth period due to soil moisture drawdown by growing vegetation, and finally started to rise once the vegetation senesced. Interannual variability of soil moisture was higher during the beginning of the growing season, affecting planting times for croplands. Precipitable water vapor was able to capture seasonal

and intra-seasonal atmospheric water vapor across cropland sites. It was also able to differentiate unimodal and bimodal growing seasons in the study region.

Actual evapotranspiration (ETa) derived from simple surface energy balance model was sensitive to rainfall dynamics. It tracked well both the unimodal and bimodal spatial and temporal rainfall patterns in the region. Both the unimodal and bimodal ETa time series were fitted by the quadratic model better than with cumulative vapor days. Moisture times to peak (MTPs) showed strong correspondence between and among land surface variables. The lags and co-occurrences between and among these land surface variables occurred in logical sequences.

Global circulation patterns and climate modes linked to the Pacific and Indian Oceans, such as El Niño Southern Oscillation (ENSO) and the Indian Ocean Dipole (IOD) modes affect rainfall in Eastern Africa. The biophysical and geophysical variables derived from passive microwave data responded to ENSO and IOD events occurring during the study period, including major floods (2006, 2010) and an extreme drought (2015).

The correspondence between passive microwave land surface parameters and crop production and crop yield was not straightforward. The spatial resolution of satellite passive microwave data and the areal units of crop production statistical data in Ethiopia is roughly similar. We addressed the spatial overlay mismatch between the AMSR pixel and crop production area through an areal normalization process. However, key limitations of the crop production data include data uncertainty and the lack of high quality, long-term data at the woreda (district) level. Data access is highly centralized at the federal level. Crop production data from the Ethiopian Statistical Agency (CSA) is not well characterized, and access to data below the zone level is restricted. The correspondence between the passive microwave data metrics and crop production data at the woreda level was encouraging, but these data were made available from a regional agricultural office through personal communication.

In contrast, the correspondence between passive microwave data metrics with crop production data at zone level (using data from CSA) was very weak, with no correspondence at some sites. Note that the woreda level analysis is correspondence across space in one year (2014), while the zone level analysis is correspondence in time (2003–2008 & 2010). According to the CSA, small holder peasant agricultural crop production data in the study zones in Northwestern Ethiopia has reportedly more than doubled in just eight years. This figure strains credulity given the interannual variation in precipitation. However, we acknowledge that the mixture of other land covers with croplands within the 25 km AMSR-E pixel may contribute to the discrepancies of the LSP product with crop production data. While the passive microwave products are found to be relevant for the study of cropland dynamics, additional study is needed to understand how they can best be used. Access to crop production and yield statistical data at the village level and the synergistic use of VNIR vegetation index data might complement such research efforts.

Acknowledgments: This research was supported in part by NASA grants NNX13AN58H & NNX14AJ32G. The AMSR-E data were accessed from the Numerical Terradynamic Simulation Group (NTSG) (http://files.ntsg.umt.edu/data/LPDR_v2/). The ETa data were provided by Dr. Gabriel Senay (U.S. Geological Survey (USGS), the Earth Resources Observation and Science (EROS) Center, the North Central Climate Science Center, Fort Collins, CO, USA; senay@usgs.gov). The TRMM data were accessed from ftp://disc2.nascom.nasa.gov/ftp/data/s4pa//TRMM_L3/TRMM_3B42_daily/. The crop production data at Zone level were accessed from Ethiopian Central Statistical Agency (CSA), and at Woreda level from Amhara National Regional State Bureau of Agriculture (personal communication), Ethiopia.

Author Contributions: W.G.A. and G.M.H conceived and designed the experiments; W.G.A. performed the experiments; W.G.A. and G.M.H. analyzed the data; W.G.A. and G.M.H. wrote the paper.

Conflicts of Interest: The authors declare no conflicts of interest.

Appendix A.

Table A1. Main institutional change periods and their description presented in Figure 17 legends for Ethiopia (Figure 17a) and Tanzania (Figure 17b).

Legend Label	Year	Description
		Ethiopia (Figure 16a)
1	1974	The Derg regime came to power. In 1975 the "Land to the Tiller" policy was declared, which granted to tenant farmers ownership on the lands they cultivated, with the objective of increasing cultivated area [94]. At the same time, there was huge national afforestation program, which may have reduced the area of marginal croplands.
2	1991	Tigray People Liberation Front (TPLF)-led Ethiopian People Revolutionary Democratic Front (EPRDF) came to power.
3	1994	The "Agriculture-Led Industrialization" (ADLI) policy was declared, which aimed at giving more resources to farmers and farm activity compared to urban dwellers and industrial and tertiary activities [97]. This change may have triggered expansion of cultivated lands on formerly uncultivated or preserved lands. Many of the lands forested during the Derg regime were abandoned and left to local farmers.
4	1995	The new constitution of 1995 approved and confirmed the state ownership of all land in Ethiopia, reversing the 1975 policy. As the land was owned by government, farmers had only use rights. This policy brought tenure insecurity to farmers and triggered a "tragedy of the commons" mentality: tenant farmers were reluctant to manage well the lands they cultivated or to invest in long-term agricultural production activity projects [97].
5	2010	"Growth and Transformation Plan" was a medium-term strategic framework for the five-year period from 2010/11 to 2014/15. During this time the "Arab Spring" revolt occurred, and some observers have commented that this plan aimed to divert attention of the Ethiopian population [98]. Execution of this plan was poor. For example, among the ten mega-sugar factories planned, not one was completed by the end date [98].
		Tanzania (Figure 16b)
B	1985	Nyerere handed power over to Ali Hassan Mwinyi [99].
C	1995	Benjamin William Mkapa was sworn in as the new president of Tanzania in the first multi-party election [99].
D	2005	Jakaya Mrisho Kikwete was elected fourth president for a five-year term.
E	2015	John Magufuli elected as fifth president of Tanzania [99].
F	1967/68	Arusha declaration; Ujamaa and Villagization. Nyerere introduced African socialism, or Ujamaa, literal meaning "family-hood" [100].
G	1980	Economic Liberalization and the National Agricultural Policy [100].
H	1990	Investment Promotion and the Transition to Multipartyism [100].
I	1995	National land policy enacted [101]
J	1997	National land policy amended [101].
K	2001	Land Act no. 4 and village land act no. 5 enacted in 1999 become operational [101].
L	2004	Land Act no. 4 and village land act no. 5 enacted in 1999 amended [101].
M	2007	Land use plan act enacted [101].

Appendix B.

Appendix B.1. Seasonal Kendall Test for Rainfall in Ethiopia

Two-Sided Homogeneity Test					
H0: S = 0 (no trend)					
HA: S != 0 (monotonic trend)					
Statistics for individual seasons					
	S	Var S	Z	tau	*p*-value
1	56	20020	0.4	0.036	0.692
2	−	20020	−2.0	−0.183	0.046
3	−102	20020	−0.7	−0.066	0.471
4	−78	20020	−0.6	−0.051	0.581
5	6	20020	0.0	0.004	0.966
6	−208	20020	−1.5	−0.135	0.142
7	−366	20020	−2.6	−0.238	0.010
8	−166	20020	−1.2	−0.108	0.241
9	−120	20020	−0.8	−0.078	0.396
10	−6	20020	0.0	−0.004	0.966
11	−88	20020	−0.6	−0.057	0.534
12	28	20020	0.2	0.018	0.843
Statistics for total series					
	S	Var S	Z	tau	*p*-value
1	−1326	240240	−2.7	−0.072	0.007
Seasonal Sen's slope and intercept					
slope: −0.0925 mm/month					
intercept: 104.3255					
number of observations: 672					

Appendix B.2. Seasonal Kendall Test for Rainfall in Tanzania

Two-Sided Homogeneity Test					
H0: S = 0 (no trend)					
HA: S != 0 (monotonic trend)					
Statistics for individual seasons					
	S	Var S	Z	tau	*p*-value
1	18	20020	0.1	0.012	0.899
2	−214	20020	−1.5	−0.139	0.130
3	−108	20020	−0.8	−0.070	0.445
4	−266	20020	−1.9	−0.173	0.060
5	−168	20020	−1.2	−0.109	0.235
6	0	20020	0.0	0.000	1.000
7	−226	20020	−1.6	−0.147	0.110
8	76	20020	0.5	0.049	0.591
9	80	20020	0.6	0.052	0.572
10	112	20020	0.8	0.073	0.429
11	−48	20020	−0.3	−0.031	0.734
12	−66	20020	−0.5	−0.043	0.641
Statistics for total series					
	S	Var S	Z	tau	*p*-value
1	−810	240240	−1.7	−0.044	0.098
Seasonal Sen's slope and intercept					
slope: −0.0362 mm/month					
intercept: 81.0414					
number of observations: 672					

References

1. FAO. FAOSTAT. Available online: http://faostat.fao.org/site/567/default.aspx#ancor (accessed on 24 August 2012).
2. Becker-Reshef, I.; Justice, C.; Sullivan, M.; Vermote, E.; Tucker, C.; Anyamba, A.; Small, J.; Pak, E.; Masuoka, E.; Schmaltz, J.; et al. Monitoring global croplands with coarse resolution earth observations: The Global Agriculture Monitoring (GLAM) project. *Remote Sens.* **2010**, *2*, 1589–1609. [CrossRef]
3. Brown, M.E.; de Beurs, K.; Vrieling, A. The response of African land surface phenology to large scale climate oscillations. *Remote Sens. Environ.* **2010**, *114*, 2286–2296. [CrossRef]
4. Adhikari, U.; Nejadhashemi, A.P.; Woznicki, S.A. Climate change and Eastern Africa: A review of impact on major crops. *Food Energy Secur.* **2015**, *4*, 110–132. [CrossRef]
5. Funk, C.; Dettinger, M.D.; Michaelsen, J.C.; Verdin, J.P.; Brown, M.E.; Barlow, M.; Hoell, A. Warming of the Indian Ocean threatens eastern and southern African food security but could be mitigated by agricultural development. *Proc. Natl. Acad. Sci. USA* **2008**, *105*, 11081–11086. [CrossRef] [PubMed]
6. Korotayev, A.; Zinkina, J. East Africa in the Malthusian trap? *J. Dev. Soc.* **2015**, *31*, 385–420. [CrossRef]
7. Barton, A. Deforestation in Ethiopia. Available online: http://www.czp.cuni.cz/knihovna/SD_Case_Studies.pdf#page=227 (accessed on 30 June 2017).
8. Dixon, J.; Gulliver, A.; Gibbon, D. *Farming Systems and Poverty: Improving Farmers' Livelihoods in a Changing World*; FAO and World Bank: Rome, Italy, 2001; p. 407.
9. Wang, G.; Schimel, D. Climate change, climate modes, and climate impacts. *Annu. Rev. Environ. Resour.* **2003**, *28*, 1–28. [CrossRef]
10. Behera, S.K.; Luo, J.J.; Masson, S.; Delecluse, P.; Gualdi, S.; Navarra, A.; Yamagata, T. Paramount impact of the Indian Ocean dipole on the east African short rains: A CGCM study. *J. Clim.* **2005**, *18*, 4514–4530. [CrossRef]
11. Funk, C.; Hoell, A.; Shukla, S.; Bladé, I.; Liebmann, B.; Roberts, J.B.; Robertson, F.R.; Husak, G. Predicting East African spring droughts using Pacific and Indian Ocean sea surface temperature indices. *Hydrol. Earth Syst. Sci.* **2014**, *18*, 4965–4978. [CrossRef]
12. Black, E. The relationship between Indian Ocean sea–surface temperature and East African rainfall. *Philos. Trans. R. Soc. A Math. Phys. Eng. Sci.* **2005**, *363*, 43–47. [CrossRef] [PubMed]
13. Owiti, Z.; Ogallo, L.A.; Mutemi, J. Linkages between the Indian Ocean dipole and east African seasonal rainfall anomalies. *J. Kenya Meteorol. Soc.* **2008**, *2*, 3–17.
14. Nicholson, S.E. Long-term variability of the east African 'short rains' and its links to large-scale factors. *Int. J. Climatol.* **2015**, *35*, 3979–3990. [CrossRef]
15. Williams, C.A.; Hanan, N.P. ENSO and IOD teleconnections for African ecosystems: Evidence of destructive interference between climate oscillations. *Biogeosciences.* **2011**, *8*, 27–41. [CrossRef]
16. Marchant, R.; Mumbi, C.; Behera, S.; Yamagata, T. The Indian Ocean dipole—The unsung driver of climatic variability in east Africa. *Afr. J. Ecol.* **2007**, *45*, 4–16. [CrossRef]
17. Hoell, A.; Funk, C. Indo-Pacific sea surface temperature influences on failed consecutive rainy seasons over eastern Africa. *Clim. Dyn.* **2014**, *43*, 1645–1660. [CrossRef]
18. Hoell, A.; Funk, C.; Zinke, J.; Harrison, L. Modulation of the southern Africa precipitation response to the El Niño Southern Oscillation by the subtropical Indian Ocean dipole. *Clim. Dyn.* **2016**, *48*, 2529–2540. [CrossRef]
19. Meyers, G.; McIntosh, P.; Pigot, L.; Pook, M. The years of El Niño, La Niña, and interactions with the tropical Indian Ocean. *J. Clim.* **2007**, *20*, 2872–2880. [CrossRef]
20. Schreck, C.J.; Semazzi, F.H.M. Variability of the recent climate of eastern Africa. *Int. J. Climatol.* **2004**, *24*, 681–701. [CrossRef]
21. Nicholson, S.E.; Kim, J. The relationship of the El Niño–Southern Oscillation to African rainfall. *Int. J. Climatol.* **1997**, *17*, 117–135. [CrossRef]
22. Souverijns, N.; Thiery, W.; Demuzere, M.; Lipzig, N.P.M.V. Drivers of future changes in east African precipitation. *Environ. Res. Lett.* **2016**, *11*, 114011. [CrossRef]
23. Saji, N.H.; Goswami, B.N.; Vinayachandran, P.N.; Yamagata, T. A dipole mode in the tropical Indian Ocean. *Nature* **1999**, *401*, 360–363. [CrossRef] [PubMed]

24. Webster, P.J.; Moore, A.M.; Loschnigg, J.P.; Leben, R.R. Coupled ocean-atmosphere dynamics in the Indian Ocean during 1997–98. *Nature* **1999**, *401*, 356–360. [CrossRef] [PubMed]
25. Pervez, M.S.; Henebry, G.M. Spatial and seasonal responses of precipitation in the Ganges and Brahmaputra river basins to ENSO and Indian Ocean Dipole modes: Implications for flooding and drought. *Nat. Hazard. Earth Sys.* **2015**, *15*, 147–162. [CrossRef]
26. Lyon, B.; DeWitt, D.G. A recent and abrupt decline in the east African long rains. *Geophys. Res. Lett.* **2012**, *39*, L02702. [CrossRef]
27. Brown, M.E.; de Beurs, K.M. Evaluation of multi-sensor semi-arid crop season parameters based on NDVI and rainfall. *Remote Sens. Environ.* **2008**, *112*, 2261–2271. [CrossRef]
28. Rientjes, T.; Haile, A.T.; Fenta, A.A. Diurnal rainfall variability over the Upper Blue Nile basin: A remote sensing based approach. *Int. J. Appl. Earth Obs. Geoinf.* **2013**, *21*, 311–325. [CrossRef]
29. Mathan, K.K. Influence of accumulated heat units and sunshine hours on the growth and yield of sorghum (var. Co 25). *J. Agron. Crop. Sci.* **1989**, *163*, 196–200. [CrossRef]
30. Palmer, A.H. The agricultural significance of sunshine as illustrated in California. *Mon. Weather Rev.* **1920**, *48*, 151–154. [CrossRef]
31. De Beurs, K.M.; Henebry, G.M. Land surface phenology, climatic variation, and institutional change: Analyzing agricultural land cover change in Kazakhstan. *Remote Sens. Environ.* **2004**, *89*, 497–509. [CrossRef]
32. De Beurs, K.M.; Henebry, G.M. Spatio-temporal statistical methods for modelling land surface phenology. In *Phenological Research: Methods for Environmental and Climate Change Analysis*, 2nd ed.; Hudson, I.L., Keatley, M.R., Eds.; Springer: Dordrecht, The Netherlands, 2010; pp. 177–208.
33. De Beurs, K.M.; Henebry, G.M. Northern annular mode effects on the land surface phenologies of Northern Eurasia. *J. Clim.* **2008**, *21*, 4257–4279. [CrossRef]
34. Los, S.O.; Collatz, G.J.; Bounoua, L.; Sellers, P.J.; Tucker, C.J. Global interannual variations in sea surface temperature and land surface vegetation, air temperature, and precipitation. *J. Clim.* **2001**, *14*, 1535–1549. [CrossRef]
35. Pitt, M.D.; Heady, H.F. Responses of annual vegetation to temperature and rainfall patterns in northern California. *Ecology* **1978**, *59*, 336–350. [CrossRef]
36. Morisette, J.T.; Richardson, A.D.; Knapp, A.K.; Fisher, J.I.; Graham, E.A.; Abatzoglou, J.; Wilson, B.E.; Breshears, D.D.; Henebry, G.M.; Hanes, J.M.; et al. Tracking the rhythm of the seasons in the face of global change: Phenological research in the 21st century. *Front. Ecol. Environ.* **2009**, *7*, 253–260. [CrossRef]
37. Tucker, C.J. Red and photographic infrared linear combinations for monitoring vegetation. *Remote Sens. Environ.* **1979**, *8*, 127–150. [CrossRef]
38. Benedetti, R.; Rossini, P. On the use of NDVI profiles as a tool for agricultural statistics—The case-study of wheat yield estimate and forecast in Emilia-Romagna. *Remote Sens. Environ.* **1993**, *45*, 311–326. [CrossRef]
39. Funk, C.; Budde, M.E. Phenologically-tuned MODIS NDVI-based production anomaly estimates for Zimbabwe. *Remote Sens. Environ.* **2009**, *113*, 115–125. [CrossRef]
40. Maselli, F.; Conese, C.; Petkov, L.; Gilabert, M.A. Use of NOAA-AVHRR NDVI data for environmental monitoring and crop forecasting in the Sahel—Preliminary-results. *Int. J. Remote Sens.* **1992**, *13*, 2743–2749. [CrossRef]
41. Rasmussen, M.S. Assessment of millet yields and production in northern Burkina-Faso using integrated NDVI from the AVHRR. *Int. J. Remote Sens.* **1992**, *13*, 3431–3442. [CrossRef]
42. Mkhabela, M.S.; Bullock, P.; Raj, S.; Wang, S.; Yang, Y. Crop yield forecasting on the canadian prairies using MODIS NDVI data. *Agric. For. Meteorol.* **2011**, *151*, 385–393. [CrossRef]
43. FEWS-NET. USGS FEWS NET Data Portal. Available online: http://earlywarning.usgs.gov/fews (accessed on 15 February 2017).
44. FAO. GIEWS-Global Information and Early Warning System. Available online: http://www.fao.org/giews/en/ (accessed on 15 March 2017).
45. Alemu, W.G.; Henebry, G.M. Comparing passive microwave with visible-to-near-infrared phenometrics in croplands of northern Eurasia. *Remote Sens.* **2017**, *9*, 613. [CrossRef]
46. Alemu, W.G.; Henebry, G.M. Characterizing cropland phenology in major grain production areas of Russia, Ukraine, and Kazakhstan by the synergistic use of passive microwave and visible to near infrared data. *Remote Sens.* **2016**, *8*, 1016. [CrossRef]

47. Alemu, W.G.; Henebry, G.M. Land surface phenologies and seasonalities using cool earthlight in mid-latitude croplands. *Environ. Res. Lett.* **2013**, *8*, 045002. [CrossRef]
48. Ganguly, S.; Friedl, M.A.; Tan, B.; Zhang, X.; Verma, M. Land surface phenology from MODIS: Characterization of the Collection 5 global land cover dynamics product. *Remote Sens. Environ.* **2010**, *114*, 1805–1816. [CrossRef]
49. Sakamoto, T.; Van Nguyen, N.; Ohno, H.; Ishitsuka, N.; Yokozawa, M. Spatio–temporal distribution of rice phenology and cropping systems in the Mekong delta with special reference to the seasonal water flow of the Mekong and Bassac rivers. *Remote Sens. Environ.* **2006**, *100*, 1–16. [CrossRef]
50. Zhang, X.Y.; Friedl, M.A.; Schaaf, C.B.; Strahler, A.H. Climate controls on vegetation phenological patterns in northern mid- and high latitudes inferred from MODIS data. *Glob. Chang. Biol.* **2004**, *10*, 1133–1145. [CrossRef]
51. Henebry, G.M. Phenologies of North American grasslands and grasses. In *Phenology: An Integrative Environmental Science*; Schwartz, M.D., Ed.; Springer: Berlin, Germany, 2013; pp. 197–210.
52. Henebry, G.M.; de Beurs, K.M. Remote sensing of land surface phenology: A prospectus. In *Phenology: An Integrative Environmental Science*; Schwartz, M.D., Ed.; Springer: Berlin, Germany, 2013; pp. 385–411.
53. Du, J.; Kimball, J.S.; Shi, J.; Jones, L.A.; Wu, S.; Sun, R.; Yang, H. Inter-calibration of satellite passive microwave land observations from AMSR-E and AMSR2 using overlapping FY3B-MWRI sensor measurements. *Remote Sens.* **2014**, *6*, 8594–8616. [CrossRef]
54. Senay, B.G.; Budde, M.; Verdin, P.J.; Melesse, M.A. A coupled remote sensing and simplified surface energy balance approach to estimate actual evapotranspiration from irrigated fields. *Sensors* **2007**, *7*, 979–1000. [CrossRef]
55. Senay, G.B.; Bohms, S.; Singh, R.K.; Gowda, P.H.; Velpuri, N.M.; Alemu, H.; Verdin, J.P. Operational evapotranspiration mapping using remote sensing and weather datasets: A new parameterization for the SSEB approach. *J. Am. Water Resour. Assoc.* **2013**, *49*, 577–591. [CrossRef]
56. Henebry, G.M.; de Beurs, K.M.; Wright, C.K.; Ranjeet, J.; Lioubimtseva, E. Dryland east Asia in hemispheric context. In *Dryland East Asia: Land Dynamics amid Social and Climate Change*; Chen, J., Wan, S., Henebry, G., Qi, J., Gutman, G., Sun, G., Kappas, M., Eds.; Higher Education Press and Walter de Gruyter GmbH: Berlin, Germany, 2013; pp. 23–43.
57. USGS. 30 Meter Global Land Cover. Available online: https://landcover.usgs.gov/glc/ (accessed on 29 March 2016).
58. Jones, L.A.; Kimball, J.S. Daily Global Land Surface Parameters Derived from AMSR-E. Boulder Colorado USA: National Snow and Ice Data Center. Available online: http://nsidc.org/data/nsidc-0451 (accessed on 30 June 2017).
59. Bolten, J.D.; Crow, W.T. Improved prediction of quasi-global vegetation conditions using remotely-sensed surface soil moisture. *Geophys. Res. Lett.* **2012**, *39*, L19406. [CrossRef]
60. Bolten, J.D.; Crow, W.T.; Xiwu, Z.; Jackson, T.J.; Reynolds, C.A. Evaluating the utility of remotely sensed soil moisture retrievals for operational agricultural drought monitoring. *IEEE J. Sel. Top. Appl. Earth Obs. Remote Sens.* **2010**, *3*, 57–66. [CrossRef]
61. DAAC-LP. MODIS Products Table. Land Processes Distributed Active Archive Center. Available online: https://lpdaac.usgs.gov/dataset_discovery/modis/modis_products_table (accessed on 24 December 2014).
62. TRMM. TRMM/TMPA 3B42 TRMM and Others Rainfall Estimate Data v7. Product Summary. Available online: https://mirador.gsfc.nasa.gov/collections/TRMM_3B42__007.shtml (accessed on 15 August 2015).
63. TRMM. TRMM/TMPA 3B42 TRMM and Others Rainfall Estimate Data v7. Goddard Space Flight Center Distributed Active Archive Center (GSFC DAAC), 2011. Available online: https://lpdaac.usgs.gov/dataset_discovery/modis/modis_products_table (accessed on 15 August 2015).
64. Schneider, U.; Becker, A.; Finger, P.; Meyer-Christoffer, A.; Rudolf, B.; Ziese, M. GPCC Full Data Reanalysis Version 6.0 at 1.0°: Monthly Land-Surface Precipitation from Rain-Gauges Built on GTS-Based and Historic Data. Available online: https://www.esrl.noaa.gov/psd/data/gridded/data.gpcc.html (accessed on 14 March 2017).
65. NOAA. Monthly Atmospheric and Sea Surface Temperature Indices. National Weather Service Climatic Prediction Center, 2015. Available online: http://www.cpc.ncep.noaa.gov/data/indices/sstoi.indices (accessed on 17 June 2015).

66. JAMSTEC. *Indian Ocean Dipole*, 2012 ed.; JAMSTEC: Yokosuka, Japan, 2016. Available online: http://www.jamstec.go.jp/frcgc/research/d1/iod/DATA/dmi.monthly.txt (accessed on 15 August 2015).
67. CSA. Agricultural Sample Survey, Time Series Data for National & Regional Level. Available online: http://www.csa.gov.et/images/general/news/agss_time_series%20report (accessed on 24 September 2015).
68. CSA. Ethiopian National Data Archive (ENADA). Available online: http://213.55.92.105/enada/index.php/catalog/ (accessed on 24 September 2015).
69. HarvestChoice. Agricultural Sample Survey. Available online: https://harvestchoice.org/topics/surveycensus-archive (accessed on 24 September 2015).
70. HarvestChoice. National Sample Census of Agriculture 2007/2008 Small Holder Agriculture: Regional Report. Available online: https://harvestchoice.org/search/apachesolr_search/%5BTanzania%5D%20National%20Sample%20Census%20of%20Agriculture%202007/2008%3A%20Regional%20Report (accessed on 24 September 2015).
71. McMaster, G.S.; Wilhelm, W.W. Growing degree-days: One equation, two interpretations. *Agric. For. Meteorol.* **1997**, *87*, 291–300. [CrossRef]
72. Sarma, A.; Kumar, T.V.L.; Koteswararao, K. Development of an agroclimatic model for the estimation of rice yield. *J. Indian Geophys. Union* **2008**, *12*, 89–96.
73. NOAA. Description of Changes to Oceanic Niño Index (ONI). Available online: http://www.cpc.ncep.noaa.gov/products/analysis_monitoring/ensostuff/ONI_change.shtml (accessed on 22 June 2016).
74. Bolton, D.K.; Friedl, M.A. Forecasting crop yield using remotely sensed vegetation indices and crop phenology metrics. *Agric. For. Meteorol.* **2013**, *173*, 74–84. [CrossRef]
75. Dagg, M.; Woodhead, T.; Rijks, D.A. Evaporation in east Africa. *Int. Assoc. Sci. Hydrol. Bull.* **1970**, *15*, 61–67. [CrossRef]
76. Woodhead, T. Empirical relations between cloud amount, insolation and sunshine duration in east Africa: II. *East. Afr. Agric. For. J.* **1967**, *32*, 474–477.
77. Woodhead, T. Empirical relations between cloud amount, insolation and sunshine duration in east Africa: I. *East. Afr. Agric. For.* **1966**, *32*, 211–213.
78. Gashaw, W.; Legesse, D. Flood hazard and risk assessment using GIS and remote sensing in Fogera Woreda, northwest Ethiopia. In *Nile River Basin: Hydrology, Climate and Water Use*; Melesse, A.M., Ed.; Springer: Dordrecht, The Netherlands, 2011; pp. 179–206.
79. IFRC. Ethiopia: Floods. Emergency Appeal No. MDRET003. 2006. Available online: http://www.ifrc.org/docs/appeals/06/MDRET003rev.pdf (accessed on 6 September 2006).
80. DPPA. Joint Government and Humanitarian Partners Flash Appeal for the 2006 Flood Disaster in Ethiopia. 2006; p. 25. Available online: http://www.dppc.gov.et/downloadable/reports/appeal/2006/Flood%20Appeal%20II%20MASTER%20Final.pdf (accessed on 15 June 2016).
81. UN-OCHA. Ocha Annual Report 2006: Activities and Use of Extrabudgetary Funds. Part III, Coordination Activities in the Field, Ethiopia. 2006. Available online: http://www.unocha.org/annualreport/2006/html/part3_ethiopia.html (accessed on 15 June 2016).
82. Jury, M.R. Meteorological scenario of Ethiopian floods in 2006–2007. *Theor. Appl. Climatol.* **2011**, *104*, 209–219. [CrossRef]
83. IFRC. Ethiopia: Response to Seasonal Floods. Available online: http://www.ifrc.org/docs/appeals/10/MDRET009.pdf (accessed on 28 September 2010).
84. UNCIEF. Eastern and Southern Africa: Ethiopia. Available online: https://www.ifpri.org/division/eastern-and-southern-africa-office-esao (accessed on 30 June 2017).
85. IFPRI. Ethiopia's 2015 Drought: No Reason for a Famine. Available online: http://www.ifpri.org/blog/ethiopias-2015-drought-no-reason-famine (accessed on 21 November 2016).
86. UN-WFP. Drought in Ethiopia: 10 Million People in Need. Available online: https://www.wfp.org/stories/drought-ethiopia-10-million-people-need (accessed on 21 Novemebr 2016).
87. GEOGLAM. Early Warning Crop Monitor Report. Available online: http://www.cropmonitor.org/pages/archive.php (accessed on 21 November 2016).
88. UN-OCHA. El Niño in East Africa. Available online: http://www.unocha.org/el-nino-east-africa (accessed on 21 November 2016).
89. FEWS-NET. FEWS NET El Niño Monitoring Resources. Available online: http://www.fews.net/fews-net-el-ni%C3%B1o-monitoring-resources (accessed on 21 November 2016).

90. Jones, M.O.; Jones, L.A.; Kimball, J.S.; McDonald, K.C. Satellite passive microwave remote sensing for monitoring global land surface phenology. *Remote Sens. Environ.* **2011**, *115*, 1102–1114. [CrossRef]
91. Devereux, S.; Sharp, K. Trends in poverty and destitution in Wollo, Ethiopia. *J. Dev. Stud.* **2006**, *42*, 592–610. [CrossRef]
92. FAO. *FAO Statistical Yearbook for Africa*; FAO Regional Office for Africa: Accra, Ghana, 2014; Available online: http://www.fao.org/3/a-i3620e.pdf (accessed on 30 June 2017).
93. Bewket, W. Rainfall variability and crop production in Ethiopia: Case study in the Amhara Region. In Proceedings of the 16th International Conference of Ethiopian Studies, Trondheim, Norway, 2–6 July 2007.
94. Crewett, W.; Bogale, A.; Korf, B. Land tenure in Ethiopia. Continuity and Change. Available online: http://ebrary.ifpri.org/cdm/ref/collection/p15738coll2/id/24652 (accessed on 1 September 2008).
95. Liu, Y.Y.; van Dijk, A.I.J.M.; McCabe, M.F.; Evans, J.P.; de Jeu, R.A.M. Global vegetation biomass change (1988–2008) and attribution to environmental and human drivers. *Glob. Ecol. Biogeogr.* **2013**, *22*, 692–705. [CrossRef]
96. Pohlert, T. Non-Parametric Trend Tests and Change-Point Detection. Available online: https://cran.r-project.org/web/packages/trend/vignettes/trend.pdf (accessed on 30 July 2017).
97. Gudeta, Z. How successful the Agricultural Development Led Industrialisation Strategy (ADLI) will be by leaving existing landholding system intact. *Econ. Focus* **2002**, *4*, 16–20.
98. Abbink, J. *A Decade of Ethiopia: Politics, Economy and Society 2004–2016*; Brill Publisher: Leiden, The Netherlands, 2017.
99. Wikipedia. History of Tanzania. Available online: https://en.wikipedia.org/wiki/History_of_Tanzania (accessed on 18 August 2017).
100. Ministry of Lands and Human Settlements Development. *National Land Policy*, 2nd ed.; Ministry of Lands and Human Settlements Development: Dar es Salaam, Tanzania, 1997. Available online: https://www.tanzania.go.tz/egov_uploads/documents/nationallandpolicy_sw.pdf (accessed on 30 June 2017).
101. Myenzi, Y. Trends and Issues in the Tanzania Land Tenure System and the Kilimo Kwanza Strategy. Available online: http://www.hakiardhi.org/index.php?option=com_docman&task=doc_download&gid=61&Itemid=81 (accessed on 23 February 2010).